Physics of the Earth and Planetary Interiors 246 (2015) 52–71

Contents lists available at ScienceDirect

Physics of the Earth and Planetary Interiors

journal homepage: www.elsevier.com/locate/pepi

Invited review

# Rotating convective turbulence in Earth and planetary cores

J.M. Aurnou [a,b,*], M.A. Calkins [c], J.S. Cheng [b], K. Julien [c], E.M. King [d], D. Nieves [c], K.M. Soderlund [e], S. Stellmach [f]

[a] Institut de Recherche sur les Phénomène Hors Equilibre, Marseille, France
[b] Department of Earth, Planetary & Space Sciences, University of California, Los Angeles, USA
[c] Department of Applied Mathematics, University of Colorado, Boulder, USA
[d] US Global Development Lab, US Agency for International Development, Washington, DC, USA
[e] Institute for Geophysics, University of Texas at Austin, USA
[f] Institut für Geophysik, Westfälische Wilhelms-Universität, Münster, Germany

ARTICLE INFO

*Article history:*
Received 14 December 2014
Received in revised form 7 June 2015
Accepted 10 July 2015
Available online 23 July 2015

*Keywords:*
Core dynamics
Convection
Turbulence
Dynamo theory

ABSTRACT

An accurate description of turbulent core convection is necessary in order to build robust models of planetary core processes. Towards this end, we focus here on the physics of rapidly rotating convection. In particular, we present a closely coupled suite of advanced asymptotically-reduced theoretical models, efficient Cartesian direct numerical simulations (DNS) and laboratory experiments. Good convergence is demonstrated between these three approaches, showing that a comprehensive understanding of the dynamics appears to be within reach in our simplified rotating convection system. The goal of this paper is to review these findings, and to discuss their possible implications for planetary cores dynamics.


**Contents**



* Corresponding author at: Department of Earth, Planetary & Space Sciences, UCLA, USA.
*E-mail address:* jona@epss.ucla.edu (J.M. Aurnou).

http://dx.doi.org/10.1016/j.pepi.2015.07.001
0031-9201/

## 1. Introduction

Earth's global-scale magnetic field is generated deep inside our planet, within the iron-rich core. Flows of molten metal in the liquid outer core, which are likely driven by thermo-chemical buoyancy forces, continually regenerate the geomagnetic field, creating a self-sustaining planetary dynamo. Fig. 1a shows the radial component of the geomagnetic field in 2000 A.D. plotted on the core-mantle boundary (CMB) (Jackson, 2003). In this image, the field is spatially-resolved up to spherical harmonic degree 13; higher order components are masked by the magnetization of Earth's crust (e.g., Fig. 3 in Roberts and King, 2013). The magnetic field is dominated by its axial dipolar component, with magnetic flux predominantly emerging from the southern hemisphere and returning back through the CMB in the northern hemisphere. Most of the axial dipole's energy is contained in four strong high latitude flux patches, two in the northern hemisphere and two in the southern hemisphere (e.g., Olson and Amit, 2006). These flux patches are located in the vicinity of the tangent cylinder, the imaginary axial cylinder shown schematically in Fig. 1d that circumscribes the solid inner core's equator. Magnetic flux patches exist in the vicinity of the magnetic equator as well. These equatorial flux patches also contain significant magnetic energy (Jackson, 2003). Due to their low latitude placement, they contribute principally to the higher, non-dipolar axial components of the geomagnetic field.

At present, numerical simulations form the primary tool for studying dynamo processes on Earth and the other planets (e.g., Stanley and Glatzmaier, 2010). Dynamo action develops in these simulations, primarily driven by axially-aligned columnar flows that qualitatively resemble non-magnetic rotating convection (e.g., Kageyama and Sato, 1997; Olson et al., 1999; Ishihara and Kida, 2002; Aubert et al., 2008; Soderlund et al., 2012; Sreenivasan et al., 2014). For example, Fig. 1b shows a snapshot of the radial component of the magnetic field on the outer boundary of a spherical shell dynamo simulation from the study of Soderlund et al. (2012), with resolution up to spherical harmonic degree 64. In this image, strong magnetic flux patches are evident at higher latitudes near where the tangent cylinder intersects the outer boundary. Further, strong flux patches are generated with a high degree of symmetry across the geographic equator. (For detailed descriptions of magnetic induction processes in planetary dynamos and numerical dynamo models, we refer to a number of recent review articles: Sreenivasan (2010), Jones (2011), Roberts and King (2013).)

The magnetic field in Fig. 1b is generated by simultaneously solving the evolution equations of convection-driven magnetohydrodynamic induction in a spherical shell with outer boundary $r_o$ and inner boundary $r_i$ (e.g., Glatzmaier, 2013):

$$\partial_t \mathbf{u} + (\mathbf{u}\cdot\nabla)\mathbf{u} = -\nabla p + (Ra\,Pr^{-1})\Theta(\vec{r}/r_o) + \nabla^2\mathbf{u} - E^{-1}\hat{z}\times\mathbf{u} + (E\,Pm)^{-1}(\nabla\times\mathbf{B})\times\mathbf{B}, \quad (1)$$

$$\partial_t \Theta + (\mathbf{u}\cdot\nabla)\Theta = Pr^{-1}\nabla^2\Theta, \quad (2)$$

$$\partial_t \mathbf{B} + (\mathbf{u}\cdot\nabla)\mathbf{B} = (\mathbf{B}\cdot\nabla)\mathbf{u} + Pm^{-1}\nabla^2\mathbf{B}, \quad (3)$$

subject to the solenoidal conditions $\nabla\cdot\mathbf{u} = 0$ and $\nabla\cdot\mathbf{B} = 0$ for the velocity and magnetic fields, $\mathbf{u}$ and $\mathbf{B}$, respectively. The first equation describes the conservation of momentum in a rotating

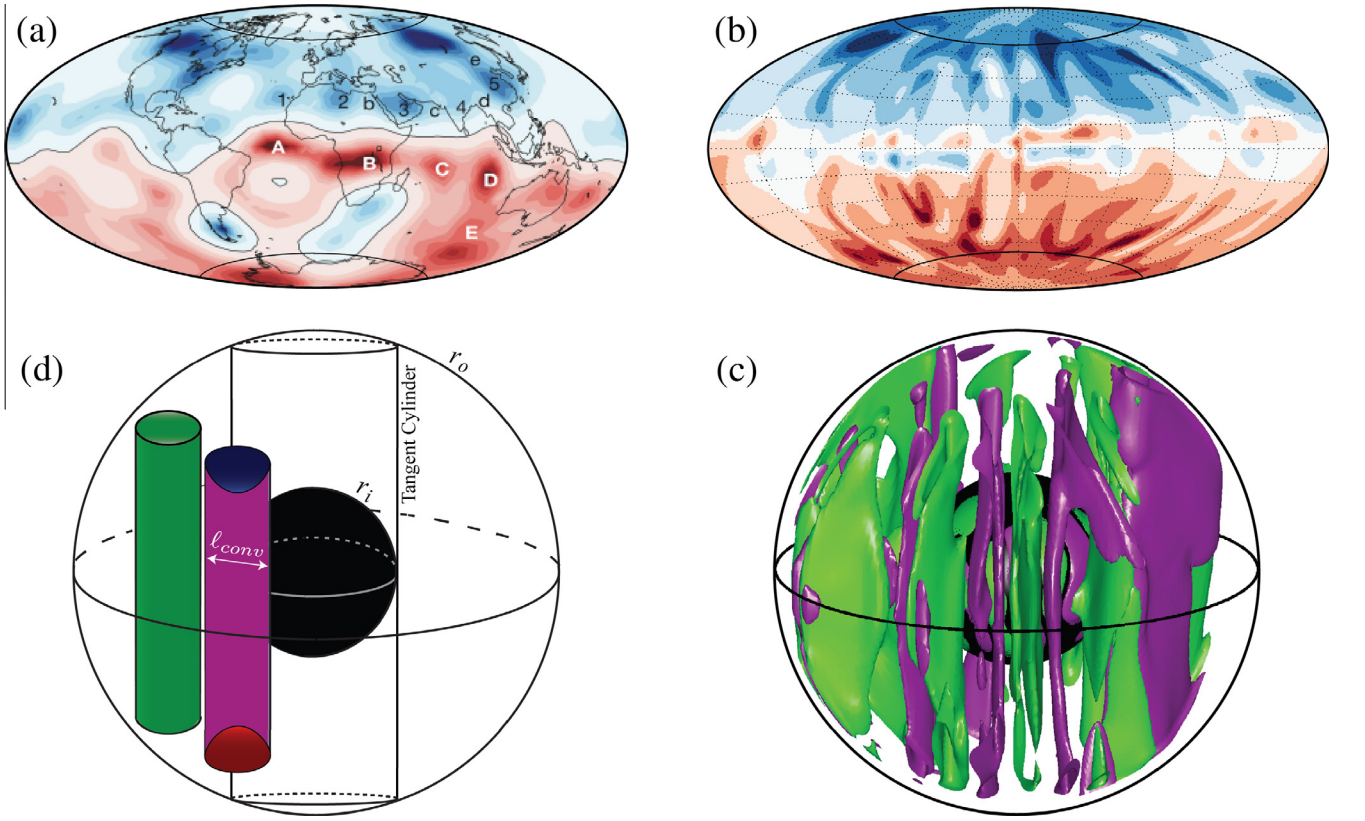


**Fig. 1.** (a) Radial magnetic field, $B_r$, on Earth's core-mantle boundary (CMB), adapted from Jackson (2003). Red (blue) denotes magnetic field parallel (antiparallel) to the radial outward normal vector. (b) Outer boundary $B_r$ from a numerical simulation by Soderlund et al. (2012); $E = 10^{-4}; Pr = 1; Pm = 2, Ra = 1.42\times10^6 = 1.9Ra_{crit}$, and radius ratio $\chi = r_i/r_o = 0.4$. The intersection of the tangent cylinder with $r_o$ is denoted by the solid black lines at $\cos^{-1}(\chi) = \pm66.4^\circ$ latitude. (c) Axial vorticity, $\zeta = \hat{z}\cdot(\nabla\times\mathbf{u})$, rendered from the same $Ra = 1.9Ra_{crit}$ case. Purple (green) denotes fluid vorticity aligned parallel (antiparallel) to the system's rotation axis. (d) Schematic of laminar axial convection columns of width $\ell_{conv}$, with associated large-scale outer boundary magnetic flux patches shown at the ends of the cyclonic columnar structure ($\zeta > 0$, purple).

shell of electrically conducting, Boussinesq fluid. The second equation is the thermal energy equation and the third is the magnetic induction equation. The dynamic pressure is demarcated by $p$ and (superadiabatic) temperature is denoted by $\Theta$.

This system of equations has been non-dimensionalized using the following scales: $H$ for length, where $H = r_o - r_i$ here denotes the fluid shell thickness (in later usages, $H$ will represent the Cartesian layer depth in $\hat{z}$); $H^2/\nu$ for time, where $\nu$ is the fluid's kinematic viscosity; $\nu/H$ for velocity; $\rho\nu^2/H^2$ for pressure, where $\rho$ is the fluid's mass density; $\Delta\Theta = \Theta(r_i) - \Theta(r_o)$ for the fixed temperature difference between the shell boundaries; $\Omega$ for the system's constant angular rotation rate, which is oriented in the axial $\hat{z}$-direction; and $\sqrt{2\rho\mu_o\eta\Omega}$ for the magnetic field, where $\mu_o$ is the magnetic permeability of free space, $\eta$ is the fluid's magnetic diffusivity, and $\Omega$ is the axial angular rotation rate of the system.

Non-dimensionalizing the system in this way then yields the following non-dimensional control parameters. The Rayleigh number $Ra = \alpha g_o \Delta\Theta H^3/(\nu\kappa)$ is the thermal and viscous time scales normalized by the squared buoyancy time scale, where $\alpha$ is the thermal expansivity and $g_o$ is the gravitational acceleration on the outer boundary. The Prandtl number $Pr = \nu/\kappa$ is the ratio of the fluid's thermal and viscous diffusion time scales. The Ekman number $E = \nu/(2\Omega H^2)$ is the system's rotation time scale, $1/(2\Omega)$, normalized by the viscous diffusion time scale. The magnetic Prandtl number $Pm = \nu/\eta$ is the ratio of the fluid's magnetic and viscous diffusion time scales, where the fluid's magnetic diffusivity $\eta = (\mu_o\sigma)^{-1}$ is the reciprocal of the magnetic permeability $\mu_o$ and the fluid's electrical conductivity $\sigma$.

Characteristic estimates of these control parameters in current-day planetary dynamo simulations, such as those of Soderlund et al. (2012) and Sreenivasan et al. (2014), are $Ra \sim 10^7$, $Pr \sim 1$, $E \sim 10^{-4}$, and $Pm \sim 1$. In contrast, characteristic values in Earth's core are $Ra \sim 10^{25}$, $Pr \sim 3 \times 10^{-2}$, $E \sim 10^{-15}$, and $Pm \sim 10^{-5}$ (Gubbins, 2001; Schubert and Soderlund, 2011). Thus, planetary dynamos and current-day numerical models of planetary dynamo action operate in disparate regions of parameter space, with most of the defining time scales differing by many orders of magnitude. It therefore remains unclear whether today's dynamo models correctly capture the leading order physical processes operating in planetary cores.

Another difficulty in building accurate models of core dynamics is that it is not possible to directly sense the velocity fields that drive the dynamo. Instead, cores flows must be inferred based on remote observations of the magnetic field itself (e.g., Pais and Jault, 2008). In contrast, one of the great strengths of numerical dynamo models is that researchers have complete information on the velocity fields that generate the model's dynamo action. For example, Fig. 1c shows a snapshot of the flow field that corresponds to the magnetic field shown in Fig. 1b. The purple surfaces in Fig. 1c show positive axial vorticity ($\zeta = \hat{z} \cdot \nabla \times \mathbf{u}$), connoting cyclonic or counterclockwise axial circulation measured in the rotating frame. The green surfaces show regions of negative axial vorticity. The boundary layers located adjacent to non-slip boundaries are not shown in this image in order to provide a clear view of the bulk convective flow. The bulk flow is dominated by axially-aligned convection columns, which roughly fill the fluid shell volume but are strongest in the region just outside the tangent cylinder. The high latitude strong magnetic flux patches are affiliated with the cyclonic vortices (purple structures in Fig. 1c). This occurs because buoyancy-driven intra-columnar flows and Ekman pumping on $r_o$ both act to generate convergent flows into the cyclonic columns, concentrating the outer boundary magnetic field in their vicinity (e.g., Olson et al., 1999; Ishihara and Kida, 2002; Aubert et al., 2008; Takahashi and Shimizu, 2012). Thus, the magnetic flux patches are found to be similar in the horizontal scales to the convection columns, and are strongest in the vicinity of the tangent cylinder where the columns tend to outcrop on $r_o$. Since roughly 10–20 columns exist in these models, a qualitatively comparable number of flux patches are generated. Further, there are radially diverging and converging flows from the columns in the equatorial plane. These near-equatorial radial flows can efficiently generate low-latitude magnetic flux patches (Bloxham, 1986), as are also evident in Fig. 1b.

Comparison of Figs. 1a and 1b shows that there is a high degree of agreement between the observed geomagnetic field morphology and the magnetic field morphologies generated in numerical dynamo models, with strong, axially-aligned flux patches at high latitudes as well as smaller-scale flux patches in the equatorial regions. This agreement between observed and surface magnetic fields in current-day planetary dynamo models, with relatively high Ekman numbers, has led to the argument, shown schematically in Fig. 1d, that the flows in present day dynamo models can be extrapolated to planetary core settings (e.g., Christensen, 2010, 2011).

However, it is not clear that the dynamo-generating flows, and the physics underlying those flows, are well understood in Earth's core. For instance, three recent studies have put forth explanations of the observed geomagnetic secular variation based, respectively, on heterogeneously-forced rotating convective flows (Aubert et al., 2013), on flows governed by so-called "magnetic winds" (Livermore et al., 2013), and by the action of stably-stratified magnetostrophic waves (Buffett, 2014). Taken as an ensemble, these studies show that the parameters describing planetary core magnetohydrodynamics (MHD) are sufficiently unconstrained that these three fundamentally different models can all provide viable explanations of the available geomagnetic data.

It is clear, though, that the flows that generate dynamo action in Earth's core must be turbulent. System-scale dynamo action can arise only if magnetic induction is capable of overcoming magnetic diffusion. The magnetic Reynolds numbers estimates this ratio on the scale of the system:

$$Rm = \frac{UH}{\eta}, \tag{4}$$

where $U$ is a characteristic velocity estimate. Dynamo action becomes possible above some critical value $Rm_{crit} = O(10)$ (cf. Christensen and Aubert, 2006; Schaeffer and Cardin, 2006). The value of $Rm$ in Earth's core is roughly estimated to be of order $10^3$, well above $Rm_{crit}$. The magnetic Reynolds number can be recast as

$$Rm = Re\,Pm, \tag{5}$$

where $Re = UH/\nu$ is the system-scale hydrodynamic Reynolds number, estimated by the ratio of the viscous diffusion time scale and the advection time scale. Flows with $Re \gtrsim 10^4$ are typically turbulent, with a broad range of length and time scales as well as cross-scale energy transfers that allow for complex cascades of energy through the system (e.g., Davidson, 2004, 2013; Mininni and Pouquet, 2010; Nataf and Schaeffer, 2015; Ouellette, 2012; Rubio et al., 2014). In Earth's core, the value of $Pm$ is estimated to be between $10^{-5}$ and $10^{-6}$ (e.g., Pozzo et al., 2012), which suggests that the Reynolds number in Earth's core is between roughly $10^8$ and $10^9$.

The core's high Reynolds number value then implies that turbulent flows exist there. However, these flows are not expected to be well described by the isotropic, homogeneous turbulence that arises in unconstrained turbulent settings (Frisch, 1995; Davidson, 2004). Instead, core turbulence is expected to be massively constrained by the action of system rotation and magnetic

fields (Julien and Knobloch, 2007; Davidson, 2013), and possibly by stratification near the boundaries (e.g., Gubbins et al., 2008; Buffett, 2014). The rotational influence on the system-scale is parameterized by the Rossby number, which is the ratio of the rotation time scale and the advection time scale,

$$Ro = \frac{U}{2\Omega H} = Re\,E, \tag{6}$$

and has estimated values ranging from $10^{-5}$ to $10^{-7}$ in Earth's core (e.g., Finlay and Amit, 2011).

In the absence of magnetic fields, the action of strong rotational forces at $Ro \ll 1$ is to impose the geostrophic force balance

$$E^{-1}\hat{z} \times \mathbf{u} \approx -\nabla p \quad \text{with} \quad \nabla \cdot \mathbf{u} = 0. \tag{7}$$

This is a pointwise diagnostic balance, which contains no dynamical information. If all other forces remain subdominant, a consequence of geostrophy is that the flow field becomes invariant over an axial scale $z$, following the Taylor–Proudman theorem (TPT), i.e., (e.g., Stewartson and Cheng, 1979; Tritton, 1988; Davidson, 2013):

$$\partial_z(\mathbf{u}, p) \approx 0. \tag{8}$$

However, geostrophy and the TPT do not imply that there are no inertial effects in low Rossby number flows. These balances are not exact: small imbalances that arise due to inertial and buoyancy forces are capable of driving turbulent fluid motions (e.g., Sprague et al., 2006; Sreenivasan and Jones, 2006b). Indeed, turbulent exchanges can still occur between small-scale inertial flows and large scale axialized modes (e.g., Julien et al., 2012b; Favier et al., 2014; Guervilly et al., 2014; Stellmach et al., 2014). When resolved in state-of-the-art simulations, these spatially anisotropic, and often spectrally non-local, exchanges can lead to novel modes of rotating convective flow (e.g., Heimpel et al., 2005; Käpylä et al., 2011; Chan and Mayr, 2013; Rubio et al., 2014) and dynamo action (Guervilly et al., 2015). This idea – that turbulent motions and fluxes are possible in low $E$, low $Ro$ settings – will prove relevant to following discussions of core convection in this manuscript.

To understand present-day dynamo modeling results as well as turbulent core flow, it is essential then to understand the physics of strongly-constrained convection. In rapidly-rotating layers of moderate $Pr \sim 1$ fluids, such as water (e.g., Grooms et al., 2010; King and Aurnou, 2012; Nieves et al., 2014) and those used in present day dynamos (e.g., Christensen and Aubert, 2006; Soderlund et al., 2012), laminar convection first occurs, or 'onsets', in the form of steady columns that are tall and narrow (e.g., Veronis, 1959; Sprague et al., 2006; Grooms et al., 2010; King and Aurnou, 2012). At convective onset, viscous forces perturb the geostrophic balance to select the narrow horizontal scale of the columns, $\ell_{conv}$ (e.g., Fig. 1d). By noting that the column height at onset, and thus the scale over which the TPT is relaxed, is predicted to be $H$, this small imbalance can be shown to be the result of vertical vorticity production through vortex stretching and vortical dissipation. These effects lead to the estimate of a convective cell with horizontal width $\ell_{conv} \sim E^{1/3}H$. In the $E \to 0$ limit, stability analyses shows that $\ell_{conv}$ varies as

$$\ell_{conv} = 2.4\,E^{1/3}H \tag{9}$$

in rotating plane layer geometry (Chandrasekhar, 1961; Julien and Knobloch, 1998). Qualitatively similar scalings are found in spherical geometries as well (e.g., Zhang and Schubert, 2000; Dormy et al., 2004).

Another source of vorticity production in planetary fluid flows can arise due to fluid compressibility. Such effects are likely of relevance in gas planets (e.g., Glatzmaier et al., 2009; Kaspi et al., 2009), and may be relevant in Earth-sized terrestrial cores as well (cf. Anufriev et al., 2005; Verhoeven and Stellmach, 2014). The effects of self-compression in liquid metal cores are not, however, considered here, but can be accurately incorporated via fully-compressible models (Calkins et al., 2014; Calkins et al., 2015a).

In present-day Cartesian models of rotating convection (Fig. 2a) and planetary dynamo action in spherical geometries (Fig. 2b), columnar convection structures follow the $E^{1/3}$ scaling predicted in (9), albeit with differing scaling coefficients (King et al., 2013; King and Buffett, 2013). These $E^{1/3}$ scalings demonstrate that these flows are geostrophically balanced at leading order. From Fig. 2b it can also be seen that the median value of the Ekman number in present-day planetary dynamos is roughly $10^{-4}$. The current community-wide understanding of core dynamo physics (e.g., Christensen, 2010) is based predominantly on the results of dynamo models carried out in the vicinity of $E \sim 10^{-4}$. At this median $E$-value, the width of convection columns is predicted by (9) to

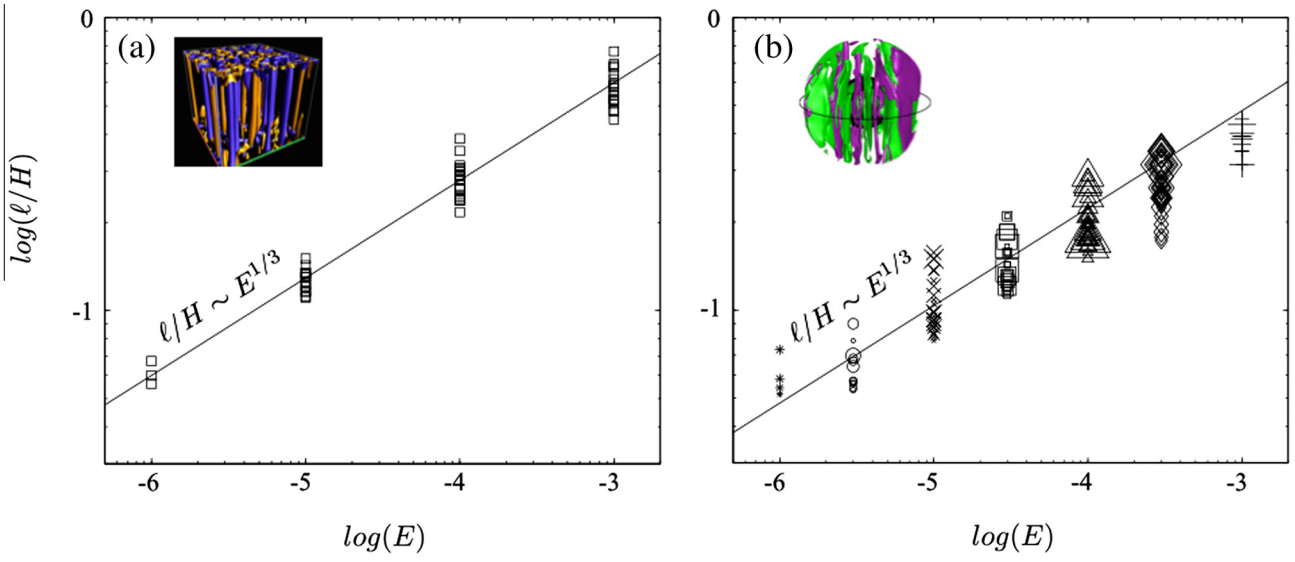


**Fig. 2.** (a) Characteristic length scales from the planar rotating convection survey studied in King et al. (2012); (b) Characteristic length scales from the spherical planetary dynamo survey studied in King and Buffett (2013).

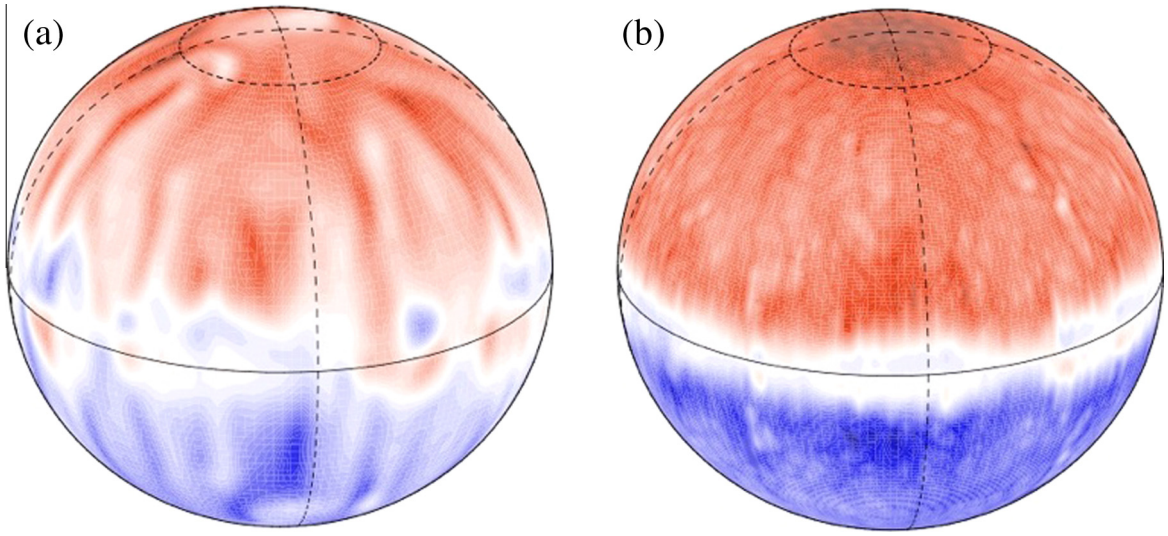


**Fig. 3.** Comparison of outer boundary radial magnetic field intensities, $B_r(r_o)$, from two dynamo simulations carried out in Sreenivasan (2010). (a) More moderate case carried out with $E = 5 \times 10^{-5}$; $Ra/Ra_{crit} = 11$; $Pr = Pm = 1$. (b) More extreme case with $E = 1.5 \times 10^{-6}$; $Ra/Ra_{crit} = 50$; $Pr = 1$, and $Pm = 0.1$. In both images, red (blue) denotes positive (negative) values. Image adapted from Sreenivasan (2010).

be $\ell_{conv}/H \simeq 0.1$. These large-scale, viscous onset columns are extremely efficient at generating large-scale magnetic fields via magnetic flux patches that are of the same scale as the columns themselves (Fig. 1b) (e.g., Olson et al., 1999).

Mapping these $E \simeq 10^{-4}$ results *directly* to Earth's core leads to the prediction of columns and associated magnetic flux patches of order 1000 km in diameter, comparable to the geomagnetic observations (Fig. 1a). However, if instead, one extrapolates (9) to Earth core conditions, where $E \simeq 10^{-15}$, this leads to the prediction that the columns would be of order 10–100 m in width. If such narrow structures are capable of existing in the core (cf. Nataf and Schaeffer, 2015), they would be far too small in scale to be geomagnetically observable.

Although such small-scale flow structures will not generate individual magnetic flux anomalies that are externally observable, this does not imply that small-scale flows are unable to take part in the large-scale dynamo generation process. In fact, a great deal of theoretical work has shown that small scale flows that have small local magnetic Reynolds numbers, $Rm_\ell = U\ell_{conv}/\eta \ll 1$, can generate ensemble electromotive forces that produce dynamo action on the large scale (e.g., Childress and Soward, 1972; Soward, 1974; Moffatt, 1978; Stellmach and Hansen, 2004; McWilliams, 2012; Roberts and King, 2013; Calkins et al., 2015b). However, the ensemble averaging of the well-organized, laminar flows that develop near the onset of rotating convection (Veronis, 1959) will tend to produce spatially uniform large-scale dynamo fields (e.g., Favier and Proctor, 2013) that are unlike the observed patchy geomagnetic field.

To illustrate the above arguments, Fig. 3 shows snapshots of the outer boundary radial magnetic field, $B_r(r_o)$, generated in two dynamo models from Sreenivasan (2010). Fig. 3a shows the results of a dynamo model with $E = 5 \times 10^{-5}$ and $Pm = 1$. In this case, large-scale convection columns generate an axial dipole field that has clear crenelations that correlate closely with the columnar flows. Fig. 3b shows $B_r(r_o)$ in a more extreme case with $E = 1.5 \times 10^{-6}$ and $Pm = 0.1$. The latter case produces a more uniform large-scale axial dipolar magnetic field, with fewer large-scale magnetic flux patches outside the tangent cylinder, dissimilar to geomagnetic observations (cf. Christensen et al., 2010). Extrapolation of these results suggests that axial columnar flows, as exist in current day models, will remain capable of generating dynamo action in the limit of low $E$ and $Pm$, but that such models will produce smooth, scale-separated large-scale magnetic fields that bear little resemblance to that of the Earth.

How then do rapidly rotating, strongly turbulent, low-$Rm_\ell$ planetary dynamos generate strong, large-scale magnetic flux patches? Similar to the geomagnetic secular variation, numerous possible answers exist to this question:

- Large-scale flux anomalies may arise due to large-scale boundary heterogeneities (Gubbins and Richards, 1986; Bloxham and Gubbins, 1987; Johnson and Constable, 1998). Recent dynamical models of these effects include the topographic CMB heterogeneity study of rapidly rotating convection by Calkins et al. (2012) and the heterogeneous buoyancy-flux driven model of the geodynamo by Aubert et al. (2013).
- It may be possible that large-scale modes of fluid motion inherently dominate core flows. For example, fixed flux boundary conditions may favor the existence of low wavenumber flows (e.g., Sakuraba and Roberts, 2009; Hori et al., 2012; Matsui et al., 2014; Cao et al., 2014, cf. Johnston and Doering (2009)).
- Constrained turbulent systems often generate large-scale flows either via energy transfer into coherent structures (e.g., McWilliams, 1984; Bardóczi et al., 2012) or through turbulent (non-diffusively-controlled) instabilities (e.g., Aurnou et al., 2003; Zimmerman et al., 2011). Large-scale magnetic flux patches may be the expression of turbulent large-scale structures in the core (e.g., Guervilly et al., 2015).
- It could even be that localized regions of intensified magnetic flux arise simply as a by-product of our remote observations of a multi-scale field. Turbulent systems typically have broad ranges of spatiotemporal complexity. Spectrally low-passed, external observations of the geomagnetic field highlight low degree flux anomalies. For examples of this phenomenon, see Fig. 4 in Calkins et al. (2012) and Fig. 4 in Roberts and King (2013).
- Lastly, it is possible that these mechanisms are convolved together in geophysical and astrophysical settings.

An accurate description of turbulent core-style convection – in particular, its essential flow behaviors and characteristic length-scales – is necessary in order to deconvolve and disambiguate the

mechanisms described above. Towards this end, we focus here on developing a better understanding of the physical processes in the case of rapidly rotating convection. In this physics-driven approach, we choose to reduce the complexity of the problem in hopes of developing a comprehensive understanding of rotating convection systems, while still retaining many key aspects of planetary core flows. In particular, we present here (i) advanced theoretical models containing the leading order physical processes in the asymptotic limit of rapid rotation; (ii) Cartesian direct numerical simulations (DNS), that can be carried out at more extreme parameter values than spherical models; and (iii) laboratory experiments capable of reaching levels of turbulence beyond what can be investigated in even the most advanced simulations. Good convergence is demonstrated between these approaches. Thus, a comprehensive understanding of the dynamics appears to be within reach in our simplified rotating convection system. The goal of this paper is to review these findings, and to discuss their geophysical implications.

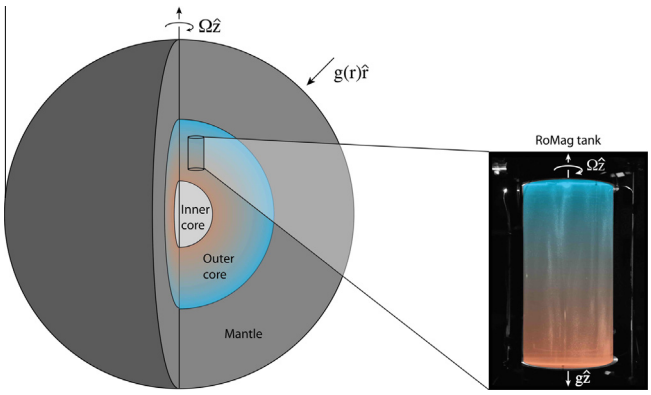


**Fig. 4.** (Left) Schematic view of Earth's interior. The coloration represents the buoyancy gradient that drives thermo-compositional convection in the iron-rich outer core fluid. (Right) Snapshot image of a laboratory rotating thermal convection experiment. Qualitatively similar to a polar region in the core (e.g., Sreenivasan and Jones, 2006a), the gravity and rotation and buoyancy gradient vectors are all axial. A laser light sheet hitting reflective flakes shows the shear structures in the rotating convective flow. Here the adverse temperature gradient is represented by the coloration, with vermilion (aquamarine) representing the warmer (cooler) fluid. Image adapted from Cheng et al. (2015).

## 2. Methods of studying rapidly-rotating convection

In this section, we present the three independent means of investigating rapidly rotating core-style convection considered here: (*i*) laboratory experiments, (*ii*) direct numerical simulations, and (*iii*) asymptotically-reduced models. In all three, core convection is simulated in a parcel of fluid located near the poles, where the gravity vector is parallel to the rotation axis (Fig. 4). The top and bottom boundaries are flat in these models. With no boundary curvature, Rossby waves do not develop and solutions do not drift in azimuth. Thus, these techniques model the fundamental rotating convection dynamics without the complexities of Rossby waves and zonal flows (e.g., Gillet et al., 2007; Calkins et al., 2012).

The capabilities of these approaches are shown schematically in Fig. 5. We posit that the intercomparison of these different meth-

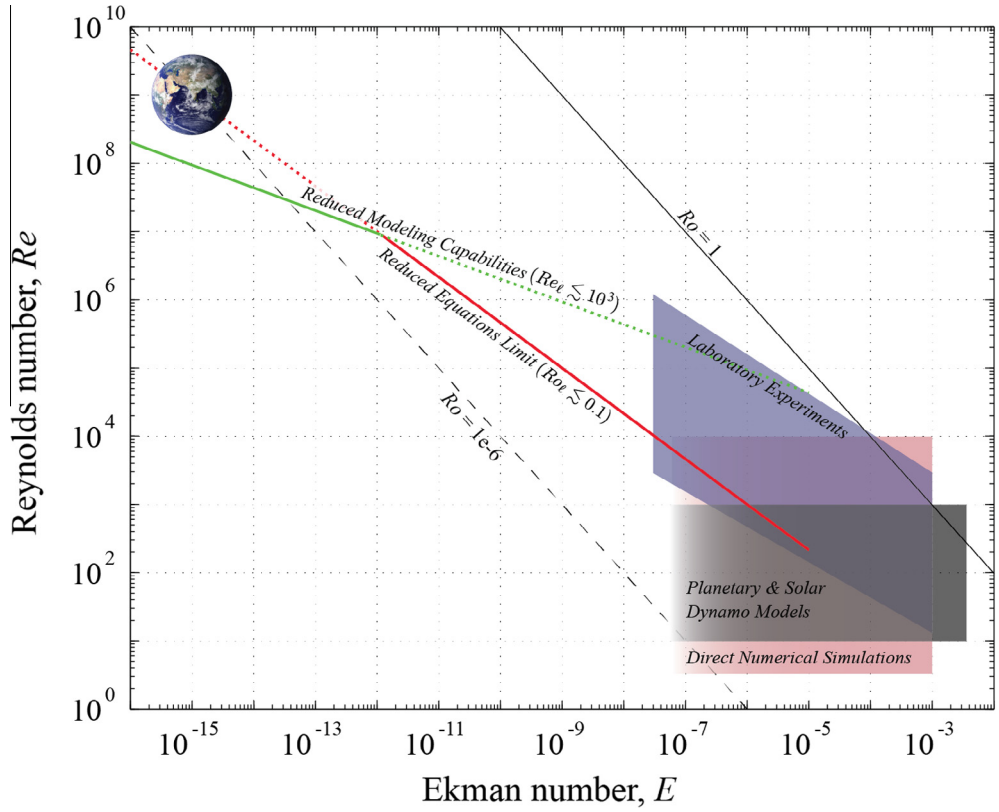


**Fig. 5.** Reynolds–Ekman regime diagram showing the different capabilities of various methods of studying rotating convection and dynamo physics. The salmon, dark grey, and deep violet colored boxes represent, respectively, the accessibility ranges of direct numerical simulations (e.g., Stellmach et al., 2014), global dynamo models (e.g., Sheyko, 2014; Jones, 2014; Nataf and Schaeffer, 2015) and rotating convection experiments in water (e.g., Cheng et al., 2015). The solid black line denotes $Ro = ReE = 1$, where geostrophic balance is expected to be lost at all scales in the fluid layer. The black dashed line corresponds to $Ro = 10^{-6}$, a typical estimate of $Ro$ in Earth's core. The red and green lines represent upper bounding limits on the reduced models, with the solid part of these lines marking the lower of the two bounds. The red line demarcates where the local $Ro_\ell = RoE^{-1/3} = 0.1$, above which the assumption of local geostrophic balance likely breaks down, thereby invalidating the reduced equations. The green line represents current-day computing capabilities for the reduced models, for which $Re_\ell \lesssim 10^3$ (e.g., Rubio et al., 2014).

**Table 1**
Non-dimensional parameters relevant for describing core turbulence, planetary dynamo models and the hydrodynamic rotating convection models described herein. In the reduced equations, the nondimensional parameters are the local Rossby $Ro_\ell$ and local Reynolds $Re_\ell$ based on the column width $\ell/H \simeq E^{1/3}$.

| System | $E$ | $Ra$ | $Pr$ | $Pm$ | $Re$ | $Ro$ |
|---|---|---|---|---|---|---|
| Earth's core | $\sim 10^{-15}$ | $\sim 10^{25}$ | $\sim 10^{-2}$ | $\sim 10^{-6}$ | $\sim 10^{8}$ | $\sim 10^{-7}$ |
| Dynamo models | $\gtrsim 10^{-6}$ | $\lesssim 10^{10}$ | 0.1–10 | $\sim 1$ | $\lesssim 10^{3}$ | $\sim 10^{-2}$ |
| Lab Experiments | $\gtrsim 10^{-8}$ | $\lesssim 10^{13}$ | 0.025–7 | 0 | $\lesssim 10^{5}$ | $\lesssim 10$ |
| Cartesian DNS | $\geqslant 10^{-7}$ | $\lesssim 10^{12}$ | 0.1–100 | 0 | $\lesssim 10^{4}$ | $\sim 10^{-2}$ |
| Reduced Models | $\lesssim 10^{-5}$ | $\lesssim 20Ra_C$ | $\sim 10^{-2}$ - $\infty$ | 0 | $Re_\ell E^{-1/3}$ | $Ro_\ell E^{1/3}$ |

ods, each with its different strengths and weaknesses, optimizes our ability to understand rotating convection physics under extreme, planetary-core-like conditions.

### 2.1. Laboratory experiments

The laboratory rotating convection experimental results presented here were made using the "RoMag" device at UCLA. RoMag consists of an upright cylindrical tank with a fixed 20 cm diameter. The tank is heated from below and cooled from above to drive thermal convection. The maximum heating power that can be passed through the system is about 5 kW. The minimum heating power is about 25 W, which, importantly, determines the minimum $Ra$ values that can be accessed in our laboratory experiments. The tank is situated on a pedestal that spins at up to 60 rotations per minute. See King et al. (2012) for further device details.

An important feature of RoMag's design is that the height of the tank's sidewall can be varied from 3.2 cm to 160 cm. The variable tank height enables data to be acquired over the broad parameter ranges (Table 1; Fig. 5) necessary to identify fundamental changes in system behavior (e.g., King et al., 2009, 2012; Cheng et al., 2015). This device uses either water or liquid gallium as the working fluid. Water has a Prandtl number $Pr \simeq 7$, comparable to the $Pr \sim 1$ values used in the vast majority of present-day dynamo models. In contrast, gallium has $Pr \simeq 0.025$ and better simulates the physical properties of metallic core fluid (King and Aurnou, 2013). In addition, gallium has a non-zero magnetic Prandtl number, $Pm \sim 10^{-6}$, and can also be used to study core-style magnetohydrodynamics. Detailed MHD convection studies are the focus of the most recent RoMag experimental surveys (e.g., King and Aurnou, 2015; Ribeiro et al., 2015), but will not be considered herein.

Hydrodynamic convection experiments allow us to characterize the core-style convective flows that underlie planetary dynamo action. To quantitatively diagnose the convection behaviors in the laboratory, simultaneous thermal field measurements are made on up to 32 thermistors. This allows us to accurately determine the Nusselt number, $Nu$, which is the non-dimensional heat transfer across the fluid layer. The Nusselt number provides a global measurement of convective heat transfer efficiency and reveals fundamental changes in convective behavioral regimes (Figs. 10 and 11). We can qualitatively determine the style of convection in water by putting optically reflective flakes into suspension. A vertical laser light sheet is used to illuminate the flakes, thereby revealing the shear structures in the flow (Fig. 7, top row). Combining thermal measurements with visualizations experiments allows us to map out differing regimes of convective flow.

### 2.2. Direct numerical simulations

Direct numerical simulations (DNS) are carried out in Cartesian domains with periodic sidewall conditions and that solve the non-magnetic ($\vec{B} = 0$) versions of Eqs. (1)–(3), subject to the solenoidal velocity condition, $\nabla \cdot \mathbf{u} = 0$, and with constant gravitational acceleration directed anti-parallel to $\hat{z}$ (Stellmach and Hansen, 2008).

In all of the DNS cases, the top and bottom boundaries are impenetrable and isothermal, with a fixed temperature difference $\Delta\Theta$ maintained between the top and bottom boundaries. Calculations using non-slip and free-slip top and bottom mechanical boundaries are both presented (Stellmach et al., 2014). In addition, an additional set of calculations is shown in which free-slip mechanical boundary conditions are augmented by a parameterized Ekman pumping condition (e.g., Greenspan, 1968). DNS are carried out here over the range $10^{-5} \geqslant E \geqslant 10^{-7}$. The width, $W$, of the computational domain is fixed at 10 onset wavelengths (for stress-free BC's), corresponding to roughly $20\,\ell_{conv}$. Using (9), the aspect ratio $\Gamma$, which is the width $W$ of the computational domain divided by its height $H$, is $\Gamma \simeq 48E^{1/3}$ for all the DNS. Thus, the DNS aspect ratios range from $\Gamma \simeq 1$ at $E = 10^{-5}$ to $\Gamma \simeq 1/5$ at $E = 10^{-7}$.

The numerical resolutions employed in the DNS reach up to $576 \times 576$ points in the horizontal directions by 513 points in the vertical direction, with a minimum of 10 grid points in the Ekman boundary layers. The code employed here has been validated by comparison with the predictions of linear theory and further benchmarked using reported results (King et al., 2012; Stellmach et al., 2014).

### 2.3. Asymptotically reduced models

In rapidly-rotating systems in which the Ekman and Rossby numbers are extremely small, as in Earth's core, it is possible to 'reduce' the governing equations to a simpler form. This can be done rigorously for rapidly rotating convection systems via a multiple scale, asymptotic expansion approach (e.g., Julien et al., 1998, 2006, 2012a,b; Sprague et al., 2006; Julien and Knobloch, 2007). Because this multiple scale asymptotic approach is not well known commonly used in the planetary interior dynamics community, we will present the essentials of this method here.

In the asymptotic expansion employed here, the small parameter $\epsilon$ is the local Rossby number $Ro_\ell$, based on the horizontal flow scale $\ell = E^{1/3}H$. Note that $\ell$ scales similarly to $\ell_{conv}$ but without the prefactor in (9) in order to maintain generality. By employing a viscous velocity scaling, $U \sim \nu/\ell$, the velocities are in local Reynolds number units, $Re_\ell = U\ell/\nu$, with horizontal components $\mathbf{u}_\perp = (u, v)$ and vertical component $w$. By substituting $U$ into the local Rossby number, we find that $Ro_\ell = \nu/(2\Omega\ell^2) = E(H/\ell)^2 = E^{1/3}$. By non-dimensionalizing the length and time scales with $\ell$ and $\ell^2/\nu$, respectively, the differentials in the Cartesian system become

$$\partial_x \to \partial_x; \quad \partial_y \to \partial_y; \quad \partial_z \to \partial_z + \epsilon\partial_Z; \quad \partial_t \to \partial_t + \epsilon^2\partial_\tau, \tag{10}$$

where $Z = \epsilon z$ is the slow spatial variable and $\tau = \epsilon^2 t$ is the slow temporal variable. Note that the axial distance over which the slow

variable, $Z$, changes by an order one value corresponds to $E^{-1/3}$ order one variations in the fast axial scale $z$. (So if $Z$ is analogous to a meter stick, then $z$ corresponds to the millimeter scale markings on the stick, providing an example of an 1000-fold difference between the fast and slow axial scales. In our multi-scale reduced environment, a similar 1000-fold scale separation describes QG convection occurring at $E \simeq 10^{-9}$.)

The temperature field is decomposed into mean and fluctuating components

$$\Theta = \overline{\Theta}(Z,\tau) + \epsilon\,\theta(x,y,z,t,Z,\tau), \tag{11}$$

where $\theta$ denotes the fluctuating temperature field and $\overline{\Theta}$ represents the mean temperature field that can vary only on the slow scales, $Z$ and $\tau$. The overbar, therefore, denotes an average over the fast scales, $x$, $y$, $z$, and $t$.

A natural consequence of employing multiple scale asymptotics is an increase in the dimensionality of the system, from four dimensions $(x, y, z, t)$ to six dimensions $(x, y, z, t, Z, \tau)$ in the current context. Indeed, the multiple scale asymptotic approach outlined here is typically referred to as the "many-variable method" (Nayfeh, 1973). However, the new slow temporal and spatial variables are not strictly independent of the original fast variables, e.g., $Z = \epsilon z$ (Bender and Orszag, 1999). Moreover, by introducing these new slow variables, the multi-scales approach helps to elucidate the physics contained within a given problem by, for example, identifying processes that occur on the fast timescale $t$ (e.g., convection) versus those that occur on the slow timescale $\tau$ (e.g., adjustment of the mean temperature profile).

At leading order, $O(\epsilon^{-1})$, the asymptotic expansion of the governing equations produces geostrophic balance:

$$\hat{z}\times\mathbf{u}_\perp = -\nabla_\perp p \quad \text{such that} \quad \mathbf{u}_\perp = (-\partial_y p, \partial_x p, 0). \tag{12}$$

From this, the axial vorticity $\zeta = \nabla\times\mathbf{u}_\perp$ can be related to the pressure field as

$$\zeta = \nabla_\perp^2 p. \tag{13}$$

It should be noted that for geostrophically balanced flows, the pressure field is formally equivalent to the geostrophic streamfunction, $\mathbf{u}_\perp = (\partial_y\psi, -\partial_x\psi)$, making it possible to replace $p$ with $\psi$ (e.g., Vallis, 2006).

This leading order solution requires that the flow remains in geostrophic balance everywhere in the fluid layer. However, it is not prognostic since it contains no time derivatives. To gain prognostic information, it is necessary to go to $O(\epsilon^0)$ in the asymptotic expansion, where evolution equations are recovered for the axial vorticity, $\zeta$, and the axial velocity, $w$:

$$\partial_t\zeta + (\mathbf{u}_\perp\cdot\nabla)\zeta = \partial_Z w + \nabla_\perp^2\zeta, \tag{14}$$

$$\partial_t w + (\mathbf{u}_\perp\cdot\nabla)w = -\partial_Z p + (\widetilde{Ra}\,Pr^{-1})\,\theta + \nabla_\perp^2 w. \tag{15}$$

Here $\widetilde{Ra} = RaE^{4/3}$ is the reduced Rayleigh number. This parameter is related to the supercriticality of the system, noting that the critical $Ra$ for Cartesian rotating convection is $Ra_{crit} = c_1 E^{-4/3}$, where the coefficient $c_1$ varies as a function of $E$ (Chandrasekhar, 1961) and reaches a value of 8.69 as $E\to 0$ (Chandrasekhar, 1961; Julien and Knobloch, 1998). Thus, we can express the reduced Rayleigh number as $\widetilde{Ra} \simeq 8.7 Ra/Ra_{crit}$.

Eqs. (14) and (15) arise because of $O(\epsilon)$ departures in geostrophic balance (12) are generated by inertial, viscous and buoyancy forces. These departures remains small and geostrophy is sustained as the leading order balance provided that the velocity amplitudes are less than $O(\epsilon^{-1})$ (Sprague et al., 2006). It follows that the large scale Reynolds number $Re_H < O(\epsilon^{-2})$. Thus, turbulent fluid motions are accessible and are to be expected in this regime.

Evolution equations for the temperature field are also required. The fluctuating and mean temperature field equations are found, respectively, at $O(\epsilon^1)$ and $O(\epsilon^2)$ to be:

$$\partial_t\theta + (\mathbf{u}_\perp\cdot\nabla)\theta = -w\partial_Z\overline{\Theta} + Pr^{-1}\nabla_\perp^2\theta, \tag{16}$$

$$\partial_\tau\overline{\Theta} = -\partial_Z(\overline{w\theta}) + Pr^{-1}\partial_Z^2\overline{\Theta}, \tag{17}$$

where, again, the overbar denotes an average over the fast time and spatial scales, $(x, y, z, t)$.

Eqs. (14)–(17) are the reduced equations for rapidly rotating convection in a plane layer geometry. Substituting the streamfunction $\psi$ for pressure, and using relationships (12) and (13), we arrive at this closed set of equations for axial vorticity, axial velocity, temperature fluctuation and mean temperature:

$$\partial_t(\nabla_\perp^2\psi) + J[\psi,\nabla_\perp^2\psi] = \partial_Z w + \nabla_\perp^4\psi, \tag{18}$$

$$\partial_t w + J[\psi, w] = -\partial_Z\psi + (\widetilde{Ra}\,Pr^{-1})\,\theta + \nabla_\perp^2 w, \tag{19}$$

$$\partial_t\theta + J[\psi,\theta] = -w\partial_Z\overline{\Theta} + Pr^{-1}\nabla_\perp^2\theta, \tag{20}$$

$$\partial_\tau\overline{\Theta} = -\partial_Z(\overline{w\theta}) + Pr^{-1}\partial_Z^2\overline{\Theta}. \tag{21}$$

Here the horizontal advection of a generic field $f$ is expressed using the Jacobian, $J[\psi,f] = \partial_x\psi\partial_y f - \partial_y\psi\partial_x f = \mathbf{u}_\perp\cdot\nabla_\perp f$. The fast axial scale $z$ does not explicitly appear in the reduced equation set as a consequence of the TPT and the averaging procedure. In addition, the fluctuating Eqs. (18)–(20) depend on the fast scales and must be timestepped over the fast time scale $t$, whereas the mean temperature Eq. (21) depends solely upon the slow scales $Z$ and $\tau$, and needs only to be timestepped on the slow time scale $\tau$. A detailed treatment of the derivation can be found in Sprague et al. (2006).

These so-called *generalized non-hydrostatic quasi-geostrophic equations* are solved here subject to fixed-temperature thermal boundary conditions

$$(\overline{\Theta} = 1,\ \theta = 0) \quad \text{at} \quad Z = 0; \quad \text{and} \quad (\overline{\Theta} = 0,\ \theta = 0) \quad \text{at} \quad Z = 1, \tag{22}$$

and mechanical conditions

$$w = 0 \quad \text{at} \quad Z = (0, 1), \tag{23}$$

which impose impenetrable velocity fields on the bottom and top boundaries. Inspection of (19) shows that $\partial_Z\psi = 0$ on the horizontal boundaries (where $w = 0$ and $\theta = 0$), such that the boundary flows are necessarily stress-free. The asymptotically-reduced equations are modeled in rectilinear domains using a semi-implicit, spectral code, which employs a Fourier decomposition on horizontal planes and a Chebyshev decomposition in the vertical direction (Sprague et al., 2006; Grooms et al., 2010). With present-day computing power, models of the generalized quasi-geostrophic (QG) equations have been made for Reynolds numbers up to $Re_\ell \sim 10^3$ (Fig. 5).

In contrast to the development above, the classical QG equations, first applied in atmospheric and oceanographic settings (e.g., Vallis, 2006), are restricted to flows with weak axial motions associated with axial hydrostatic balance. Despite their many successes (e.g., Busse, 1970; Aubert et al., 2003; Schaeffer and Cardin, 2006; Vallis, 2006; Calkins et al., 2012), the classical QG equations cannot model sizable axial non-hydrostatic effects or the effects of strongly sloping container boundaries. Because core convection is inherently non-hydrostatic and occurs in a thick spherical shell with strongly sloping spherical boundaries, convection in Earth's core cannot be modeled accurately with the classical quasi-geostrophic equations (Julien et al., 2006; Calkins et al., 2013). The generalized QG equations overcome the difficulties associated with the classical

QG equations, and are therefore well-suited to model rapidly rotating turbulent core-style convection.

At first glance, the generalized QG equations – called the 'reduced equations' henceforth – appear more complex than the full rotating convection equations employed in DNS. However, the reduced equations offer computational advantages over the full Navier–Stokes equations. First, the reduced equations filter out temporally-restrictive, fast inertial waves at and below the horizontal flow scale $\ell$, while retaining slow, spatially-anisotropic inertial waves. The increased computational efficiency of the reduced equations can be seen in our comparisons of DNS and reduced models; using less resources, the reduced models are capable of simulating four times the fluid volume than comparable DNS performed at $E = 10^{-7}$ (Figs. 12c,d).

Another advantage of the reduced equations is that they contain only two non-dimensional parameters, $\widetilde{Ra}$ and $Pr$, in comparison to the three parameters, $Ra, Pr$ and $E$, necessary to characterize Navier–Stokes. By asymptotically reducing the system in the low $Ro$ limit, it becomes possible to discuss the buoyancy forcing only in terms of the effective supercriticality of the flow ($\widetilde{Ra} \simeq 8.7 Ra/Ra_{crit}$) and the Prandtl number. It is not possible to deconvolve $Ra$ and $E$ in this system; they exist only via $\widetilde{Ra}$. This lack of an explicit Ekman number does not mean there are no viscous effects in the fluid. They are contained, for instance, in the horizontal Laplacian terms in (14) and (15). In fact, it is the diffusive terms that allow the reduced equations to naturally produce convective onset at the correct $E \to 0$ value of $Ra_{crit}$ and with the predicted non-dimensional horizontal scale of $2.4E^{1/3}$ (Sprague et al., 2006; Calkins et al., 2013).

Synonymous with there being no explicit value of $E$ in the reduced equations, there is also no explicit height $H$ to the fluid layer (Fig. 6). Instead, the reduced equations should appropriately describe convection for any sufficiently low $E$, low $Ro$ convective flow with the given $\widetilde{Ra}$ and $Pr$ values. Thus, we require only that $\ell/H \simeq E^{1/3}$, for any asymptotically low value of $E$. In this manuscript, numerical simulations of the reduced equations, so-called reduced models, are presented in which the horizontal size of the computational domain is 20 onset wavelengths, such that $W \simeq 40\,\ell_{conv}$. Since the reduced models are dominantly compared here against laboratory experiments and DNS made at $E = 10^{-7}$, we *elect* to display the height of the reduced modeling domain corresponding to $E = 10^{-7}$ (Fig. 6b). Thus, the reduced model visualizations are displayed with an aspect ratio $\Gamma = W/H \simeq 96E^{1/3} \simeq 0.45$ in Figs. 8 and 12.

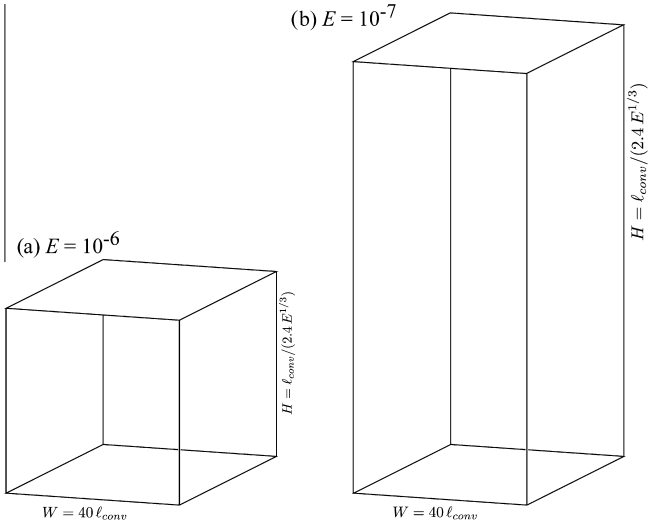


**Fig. 6.** In the reduced equations, the domain height, $H$, can be considered a variable since $E$ formally drops out of the system. Thus, $H$ can be varied for comparison with any low $E$ laboratory or DNS case. For a reduced simulation carried out using a Cartesian box that is 20 onset wavelengths wide (i.e., $W \simeq 40\,\ell_{conv}$), then, at a given $E$ value, the domain height is $H = \ell_{conv}/\left(2.4E^{1/3}\right)$. This scaling behavior is shown for (a) $E = 10^{-6}$ ($H = 1.04$ W; $\Gamma = 0.96$), and (b) $E = 10^{-7}$ ($H = 2.23$ W; $\Gamma = 0.45$). In this manuscript, reduced modeling results are rendered assuming $E = 10^{-7}$ for comparison with laboratory experiments and DNS made at this $E$ value.

The main limitations of the reduced equations presented here are that they are locally Cartesian with gravity fixed anti-parallel to the angular velocity vector; they include no Ekman pumping effects; and they are purely hydrodynamic. However, the reduced equations have been shown to be well-defined at all latitudes (Julien et al., 2006; Calkins et al., 2013). Julien et al. (2015) have recently constructed an extended reduced framework that includes the effects of Ekman pumping. Furthermore, Calkins et al. (2015b) have developed a set of multi-scale reduced MHD equations that are capable of simulating fully nonlinear dynamo action via quasi-geostrophic convection. Ongoing work is focussing on the development of a multi-scale, asymptotically reduced modeling environment in (finite) spherical geometries.

Fig. 5 shows that the reduced equations may be approaching their validity limits in Earth's core. For upper bounding estimates of the Rossby number in Earth's core, that approach $Ro \sim 10^{-5}$ (Finlay and Amit, 2011), the local scale flow may exceed $Ro_\ell \simeq 0.1$, thereby invalidating the assumption of quasi-geostrophy at all scales. If such high $Ro$ values correctly describe core flow, then it may prove necessary to develop higher order corrections to the reduced equations to accurately model small-scale core flows. Similar approaches have proven successful in the atmospheric and oceanic sciences (e.g., Gent and McWilliams, 1983).

Due to the inherent theoretical complexity in developing novel reduced equation sets, it is essential, as with any other model, to benchmark them against reference data sets. One of our goals then is to test the various assumptions underlying the generalized QG reduced equations by comparing the results of reduced models directly against those of laboratory experiments and DNS. In so doing, it is possible to show under what conditions a given asymptotically-reduced system is valid and for what conditions must they be further extended in order to be accurate (e.g., Fig. 11).

## 3. Rapidly-rotating convection results

In this section, we compare the results of laboratory experiments, which have non-slip mechanical boundary conditions (MBCs), and reduced models, with free-slip MBCs. We will further compare these against DNS with non-slip, free-slip, and so-called Ekman pumping MBCs. This exercise will show that the regime diagram of flow morphologies shows good agreement between all the methods and MBCs, with columnar flows breaking down for $Ra \gtrsim 10 Ra_{crit}$ in all $Pr = 7$ cases. However, the efficiency of rotating convective heat transfer is found to fundamentally differ under different MBCs, leading us to argue that boundary layer phenomena may play an important role in convection processes even at planetary core conditions.

### 3.1. Flow morphologies

Figs. 7 and 8 show snapshot images of the flow fields for laboratory, DNS and reduced models of rotating convection. Fig. 7 shows cases with non-slip top and bottom boundaries. The top row shows three flake visualizations from the laboratory experiments of Cheng et al. (2015), made using an 80 cm tall by

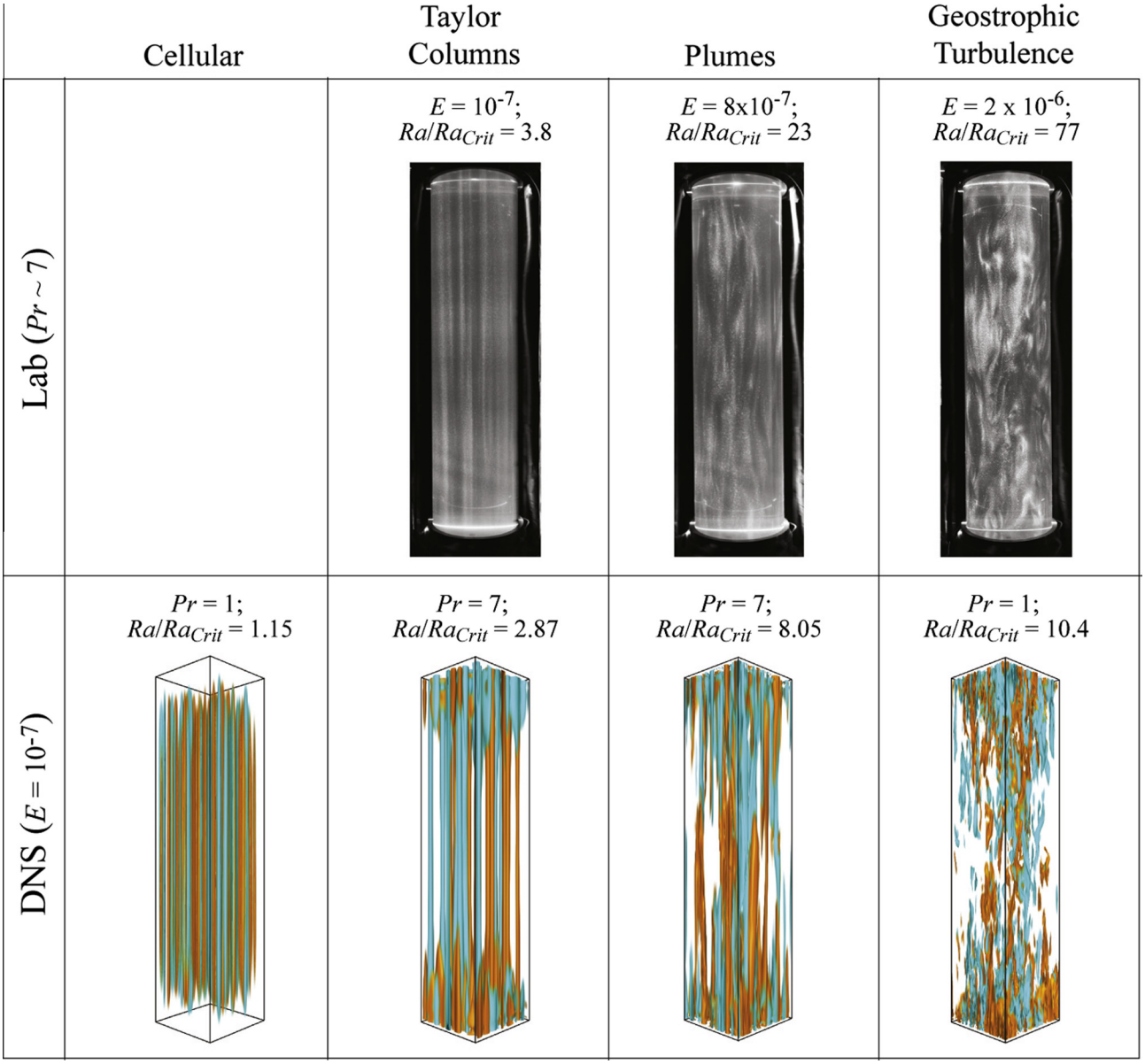


**Fig. 7.** Snapshot visualizations showing the cellular, Taylor column, plume and geostrophic turbulence regimes, as defined in Sprague et al. (2006) and Julien et al. (2012b). Top row: flake visualizations from the laboratory experiments made in Cheng et al. (2015). Bottom row: temperature fluctuation field $\theta$ from the non-slip DNS cases in Stellmach et al. (2014).

18.73 cm diameter container of water ($Pr \simeq 7$). The convection in these cases was driven by a fixed 10 W heating power, corresponding to a flux Rayleigh number $Ra_F = RaNu = 4 \times 10^{12}$. Even at this relatively low heating power, it is not possible, with water as the working fluid, to reach low enough $Ra/Ra_{crit}$ needed to access the cellular regime in the RoMag device. This inability to reach low $Ra/Ra_{crit}$ in low $E$ cases in $Pr \gtrsim 1$ fluids is a problem for all current laboratory rotating convection devices (cf. Ecke and Niemela, 2014; Cheng et al., 2015). (The opposite issue arises in $Pr \ll 1$ liquid metals, where it is more difficult to access $Ra \gg Ra_{crit}$ (e.g., Cioni et al., 2000; King and Aurnou, 2013; Ribeiro et al., 2015).)

The three laboratory images in the top row correspond to rotation rates of 60 rpm ($E = 1.2 \times 10^{-7}$), 10 rpm ($E = 7.5 \times 10^{-7}$) and 4 rpm ($E = 1.9 \times 10^{-6}$), from left to right. Since the rotation rate, and therefore $E$, is varied in each laboratory case, this leads to normalized domain widths of $W \simeq 21.0\,\ell_{conv}$ for the leftmost case; $W \simeq 10.5\,\ell_{conv}$ for the middle case; and $W \simeq 7.7\,\ell_{conv}$ for the rightmost case.

The second row in Fig. 7 shows the temperature fluctuation field, $\theta$, from non-slip DNS cases (Stellmach et al., 2014). The left and right images in this row have $Pr = 1$, while the middle two images have $Pr = 7$. The color scale is such that vermilion structures are warmer than the surrounding fluid and aquamarine structures are cooler than the surrounding fluid. This color scale is used for $\theta$ throughout this manuscript. The horizontal scale of the numerical domain is $W \simeq 20\,\ell_{conv}$ for all DNS cases reported.

Fig. 8 shows images from cases with free-slip MBCs. The top row of images from DNS made with nearly the same parameters as the non-slip DNS cases shown in Fig. 7. The bottom row shows images from the reduced models (e.g., Sprague et al., 2006; Rubio et al., 2014). Note that $Pr = 7$ in the left three images in this row, whereas $Ra/Ra_{crit} = 16.1$ in the right two cases, but the Prandtl number is lowered to $Pr = 1$ in order to boost the effective buoyancy forcing in the rightmost case shown. The horizontal scale of the numerical domain is $W \simeq 40\,\ell_{conv}$ for all of the reduced modeling results reported.

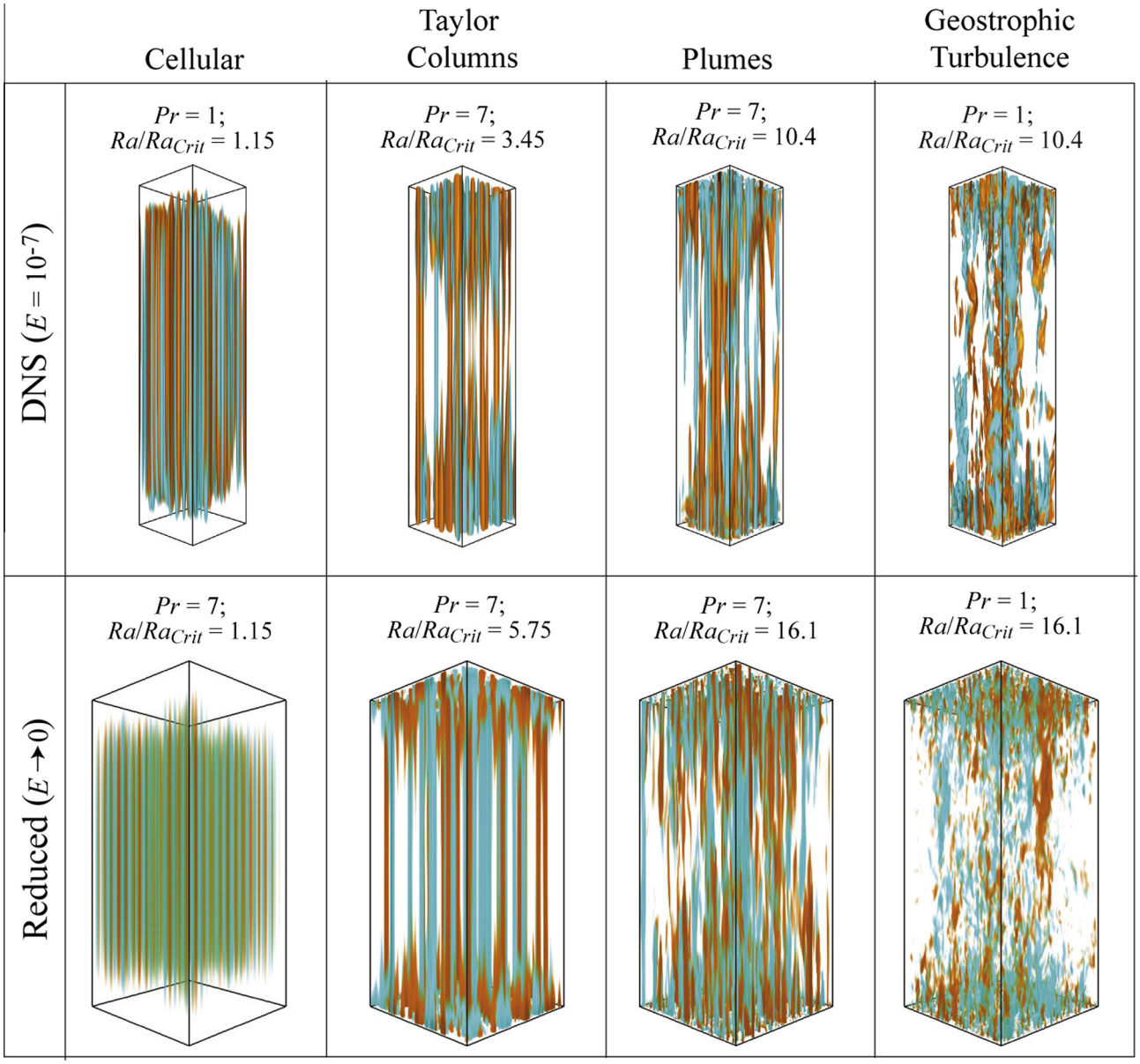


**Fig. 8.** Snapshot visualizations of the temperature fluctuation field $\theta$ for difference cases in the cellular, Taylor column, plume and geostrophic turbulence regimes, as defined in Sprague et al. (2006) and Julien et al. (2012b). Top row: free-slip DNS cases from Stellmach et al. (2014). Bottom row: Reduced modeling results from Julien et al. (2012b).

A flow morphology regime diagram is presented in the reduced modeling studies of Sprague et al. (2006) and Julien et al. (2012b). Cellular flows with horizontal widths following (9) are found close to the onset of convection, in good agreement with the seminal work of Veronis (1959). For $Pr \simeq 7$ fluid, these sinusoidal axial flow structures give way to quasi-steady, axially coherent, convective Taylor columns (CTCs) at higher supercriticality (e.g., Grooms et al., 2010; King and Aurnou, 2012; Nieves et al., 2014). CTCs form via the synchronization of convective plumes ejected from opposing thermal boundary layers. At greater forcing, this synchronization is lost, and the CTCs lose their axial coherence. This is referred to as the plume or wavy column regime. For $Pr \lesssim 1$, the cellular state transitions directly to the plume state. At still greater forcings, the convective flows lose all system-scale coherence, resulting in anisotropic 3D flows with strong variation on the convection scale, but with greater coherence in the vertical direction in comparison to the horizontal directions. This is the geostrophic turbulence regime. (In contrast, in isotropic turbulence, there is no anisotropy to the flow, with no preferred directionality to the flow field.)

The bulk flow fields in the laboratory and DNS cases qualitatively agree with those predicted by the asymptotically reduced modeling results for both non-slip and free-slip cases. (The exact regime boundaries for the no-slip cases are slightly shifted in parameter space relative to the stress-free results, as shown in Stellmach et al. (2014).) This good agreement is shown in Fig. 9, which is an adapted version of the bulk flow regime diagram of Julien et al. (2012b). The $x$-axis denotes the fluid Prandtl number. The left-hand $y$-axis shows convective supercriticality $Ra/Ra_{crit}$ and the right-hand $y$-axis is demarcated in terms of the reduced Rayleigh number $\widetilde{Ra} = (Ra/Ra_{crit})/8.7$. The different asymptotically reduced bulk flow regimes are marked here as 'C' for cells; 'T' for convective Taylor columns; 'P' denotes plumes or wavy columns; and 'G' for geostrophic turbulence. In addition, we have marked on this same plot the laboratory and DNS visualization results from Figs. 7 and 8. Laboratory experimental

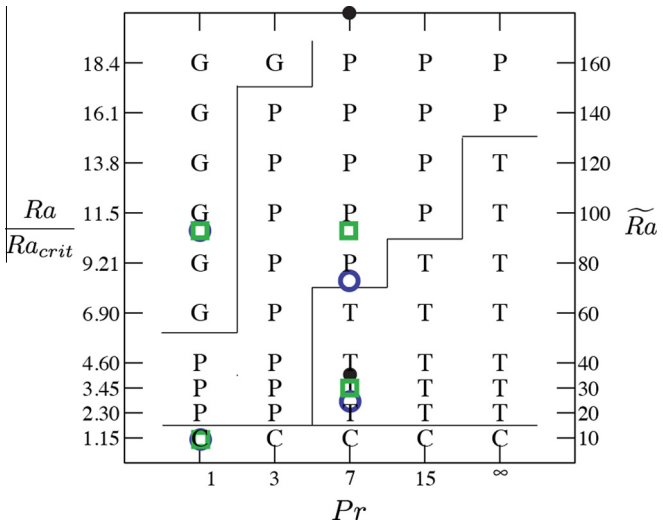


**Fig. 9.** Regime diagram ($Pr$–$Ra/Ra_{crit}$) showing regimes of bulk convective flow behavior. The asymptotically reduced morphological regimes are demarcated here as 'C' for cells, 'T' for convective Taylor columns; 'P' for plumes; and 'G' for geostrophic turbulence. Symbols represent laboratory (black filled circles) and non-slip DNS (blue, hollow circles) and free-slip DNS (green, hollow squares) visualization results. All the laboratory and DNS cases qualitatively agree with the flow regimes predicted by the asymptotically reduced modeling results.

results are marked by solid, black circles; non-slip DNS results are marked by blue, hollow circles; and free-slip DNS cases are marked by green, hollow squares.

### 3.2. Heat transfer

Fig. 10 shows measurements of rotating convective heat transfer for $Pr = 7$ fluids. The left-hand panel, Fig. 10a, shows laboratory and DNS results all carried out at $E = 10^{-7}$. The lower $x$-axis in Fig. 10a shows the non-dimensional buoyancy forcing, $Ra$, and the $y$-axis shows the non-dimensional heat transfer, $Nu$. On the top of the panel, the buoyancy force is scaled relative to the Coriolis force, forming the convective Rossby number, $Ro_C = \sqrt{\alpha g \Delta\Theta/(4\Omega^2 H)} = \sqrt{Ra E^2/Pr}$ (Gilman, 1977). This parameter is the square root of Christensen (2002)'s modified Rayleigh number, $Ro_C \simeq \sqrt{Ra^*}$. The black filled symbols show laboratory experimental data; the blue open circles show DNS results for non-slip mechanical boundary conditions; the green open squares show DNS results for free-slip boundaries.

The non-slip DNS results display a very steep heat transfer scaling over the range $2 \times 10^{10} \lesssim Ra \lesssim 5 \times 10^{10}$. The best fit trend to in this steep scaling regime is $Nu \simeq (Ra/Ra_{crit})^{3.5}$ (Cheng et al., 2015; Stellmach et al., 2014), which is the steepest rotating convective heat transfer law yet proposed (cf. King et al., 2012; Ecke and Niemela, 2014). The heat transfer behavior transitions over the range $5 \times 10^{10} \lesssim Ra \lesssim 3 \times 10^{11}$, with relatively small, but possibly non-trivial differences between the laboratory and DNS data. At still higher $Ra$ values, the laboratory data conforms to the non-rotating heat transfer $Nu \sim Ra^{2/7}$, from below. It does not overshoot the $2/7^{th}$ trend, as is often found in higher $E$ cases (Julien et al., 1996; Kunnen et al., 2006; King et al., 2012). The transition away from the steep scaling regime occurs at $Ro_C \simeq 10^{-2}$. Thus, our $E = 10^{-7}$, $Pr = 7$ data does not support a $Ro_C \simeq 1$ heat transfer transition (cf. Zhong et al., 2009).

Importantly, the free-slip DNS results follow a fundamentally different heat transfer trend, with $Nu \simeq (Ra/Ra_{crit})^{3/2}$ over the range $2 \times 10^{10} \simeq Ra \simeq 1.5 \times 10^{11}$. This scaling exponent is less than half the value of the non-slip DNS scaling. Clearly, the MBCs affect rotating convective heat transfer even at Ekman numbers as low as $E = 10^{-7}$. For instance, at $Ra \simeq 5 \times 10^{10}$, the laboratory and DNS value of $Nu$ is a factor of nearly 800% greater than the corresponding $Nu$ value for the free-slip case.

Fig. 10b shows how the convective heat transfer plotted as a function of the supercriticality of the flow $Ra/Ra_{crit}$, with the bulk flow regimes of Fig. 9 qualitatively denoted by the dashed lines at the top of the figure panel. Using $Ra/Ra_{crit}$ as the ordinate, it is formally justifiable to plot the reduced modeling results along with the DNS and laboratory results. No assumptions about the value of $E$ need be made in plotting the reduced modeling results since $Ra/Ra_{crit} = 8.696\widetilde{Ra}$. The reduced modeling results are demarcated by red x-shaped symbols. There is exceptional agreement between the free-slip DNS and the reduced modeling results for $1 \lesssim Ra/Ra_{crit} \lesssim 3.5$ (Stellmach et al., 2014). They diverge slightly for higher supercriticalities, both having heat transfer scalings trending away slightly from 3/2, which is the exponent value found in cases with $Pr \lesssim 1$ and that is theoretically predicted for rotating convective heat transfer controlled by turbulent flow in the fluid bulk (Julien et al., 2012a). Overall, quantitative measurements of convective heat transfer are in good agreement for free-slip DNS and reduced models, which approximate heat transfer in the limit of a vanishing Ekman boundary layer, whereas we find first order differences between the non-slip and free-slip $Nu$–$Ra$ data. Our studies have unexpectedly revealed that mechanical boundary effects play an important role in rotating convection at low $E$.

Fig. 11 presents additional $Nu$-$Ra/Ra_{crit}$ DNS data at $Pr = 7$, carried out to elucidate the differing heat transfer behaviors found in Fig. 10. In addition to previously displayed results, Fig. 11a contains an additional data set from Stellmach et al. (2014) that is demarcated by orange hollow squares. These orange squares mark the results of DNS made using free-slip MBCs ($\partial_z \mathbf{u}_\perp = 0$ on $z = 0, H$), as well as the effects of parameterized Ekman pumping (EP). This axial pumping condition fluxes material in and out of the boundaries according to

$$w = \pm (EH^2/2)^{1/2} \zeta \quad \text{on} \quad z = 0, H \tag{24}$$

(Niiler and Bisshopp, 1965; Greenspan, 1968), such that the axial pumping is proportional to the local axial vorticity. The EP parameterization formally violates the non-penetration condition at the top and bottom boundaries, but does so with no net flux of mass in or out of the fluid layer. The agreement in Fig. 11a between the non-slip DNS results and the free-slip EP cases demonstrates that the heat flux augmentation by boundary layer pumping explains the zeroth order differences in heat transfer scalings in Fig. 10.

Fig. 11b shows that the EP effects increase as $E$ is made smaller. To demonstrate this, we have plotted the reduced modeling results and non-slip DNS results at $E = 10^{-5}, 10^{-6}$ and $E = 10^{-7}$. At low supercriticalities, $Ra/Ra_{crit} \lesssim 2$, the $E = 10^{-7}$ non-slip DNS results are closest to the reduced modeling results. However, above $Ra/Ra_{crit} \simeq 2$, the $E = 10^{-7}$ data exceed the higher $E$ data sets, displaying the steepest local heat transfer scaling of the three $E$ cases. Thus, it appears not only that Ekman pumping is causing the difference in results between non-slip and reduced/ free-slip cases, but that this difference is exacerbated as $E$ is decreased from $E = 10^{-5}$ to $E = 10^{-7}$. It should be possible to extrapolate this result to low $E$ geophysical settings, so long as the horizontal length scale of boundary variations greatly exceeds $\ell \simeq E^{1/3} H$. Thus, we hypothesize that Ekman pumping effects may prove to be important in terrestrial planetary cores (Stellmach et al., 2014; Julien et al., 2015), while having little relevance in gas planets and stars (e.g., Julien et al., 2012a; Barker et al., 2014).

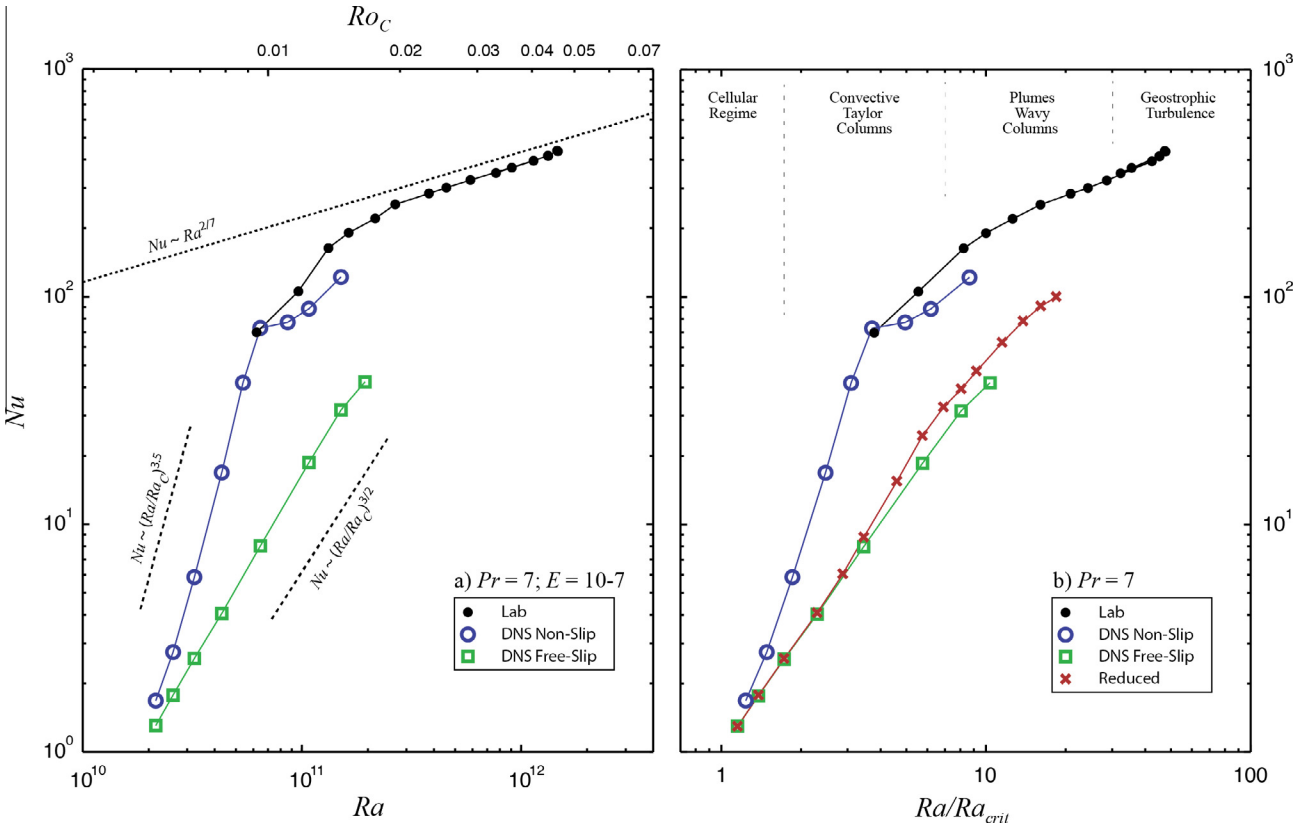


**Fig. 10.** (a) Convective heat transfer measurements ($Nu$–$Ra$) from laboratory and direct numerical simulations (DNS) carried out at $Pr = 7$ and $E = 10^{-7}$ (Stellmach et al., 2014). The dashed lines show best fit scaling trends. The $Nu \sim Ra^{2/7}$ is the best fit to non-rotating convection data not shown here (Cheng et al., 2015). The $Nu \simeq (Ra/Ra_{crit})^{3.5}$ scaling represents the best fit to the non-slip $Nu \lesssim 70$ DNS data. The $Nu \simeq (Ra/Ra_{crit})^{3/2}$ scaling represents the best fit to the free-slip DNS data. The convective Rossby number, $Ro_C$, provides a non-dimensional measure of the buoyancy forces in rotating convection systems. (b) $Nu$ as a function of supercriticality $Ra/Ra_{crit}$ from laboratory, direct numerical simulations (DNS), and asymptotically-reduced models all carried out at $Pr = 7$. Bulk flow regime boundaries, which we find are not sensitive to mechanical boundary conditions, are qualitatively shown near the top of this panel.

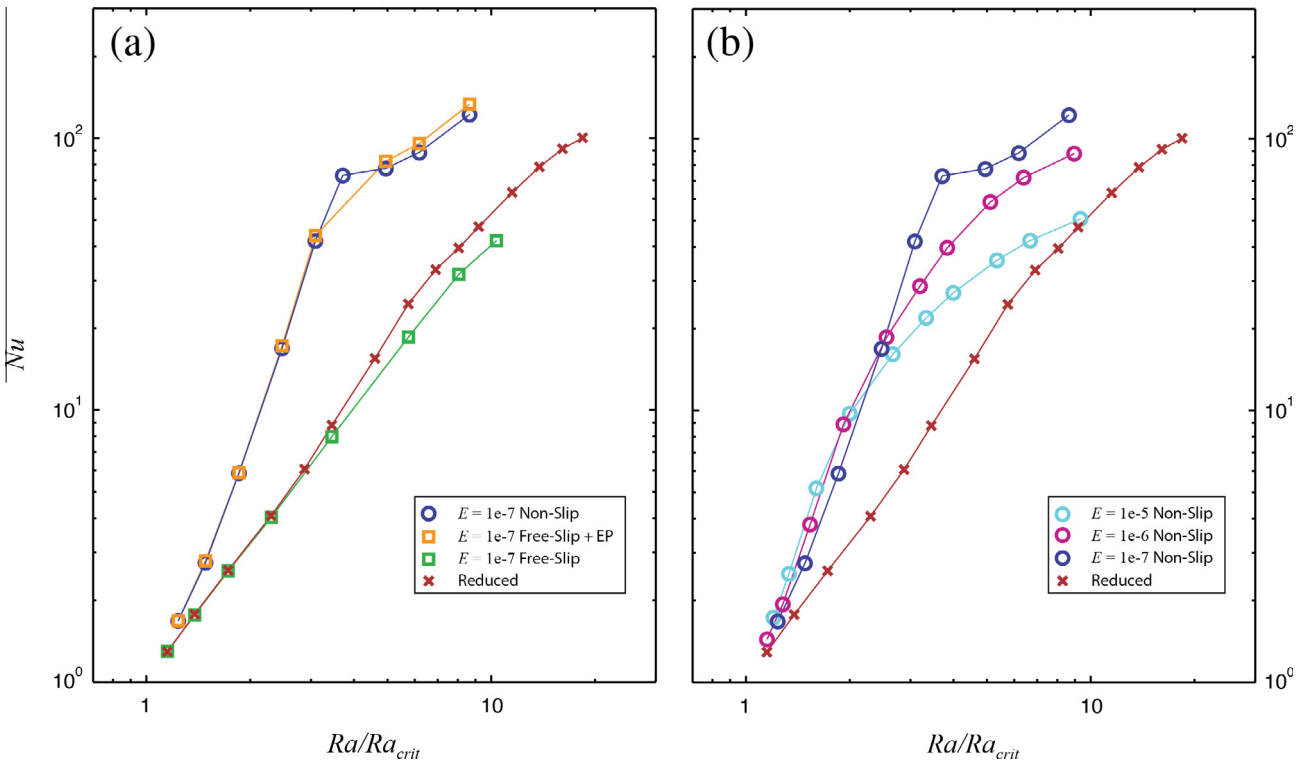


**Fig. 11.** Close up of Fig. 10b, including (a) an additional data set of DNS results made using free-slip mechanical boundary conditions and parameterized Ekman pumping (EP) and (b) additional non-slip DNS data sets at $E = 10^{-5}$ and $E = 10^{-6}$. Adapted from Stellmach et al. (2014).

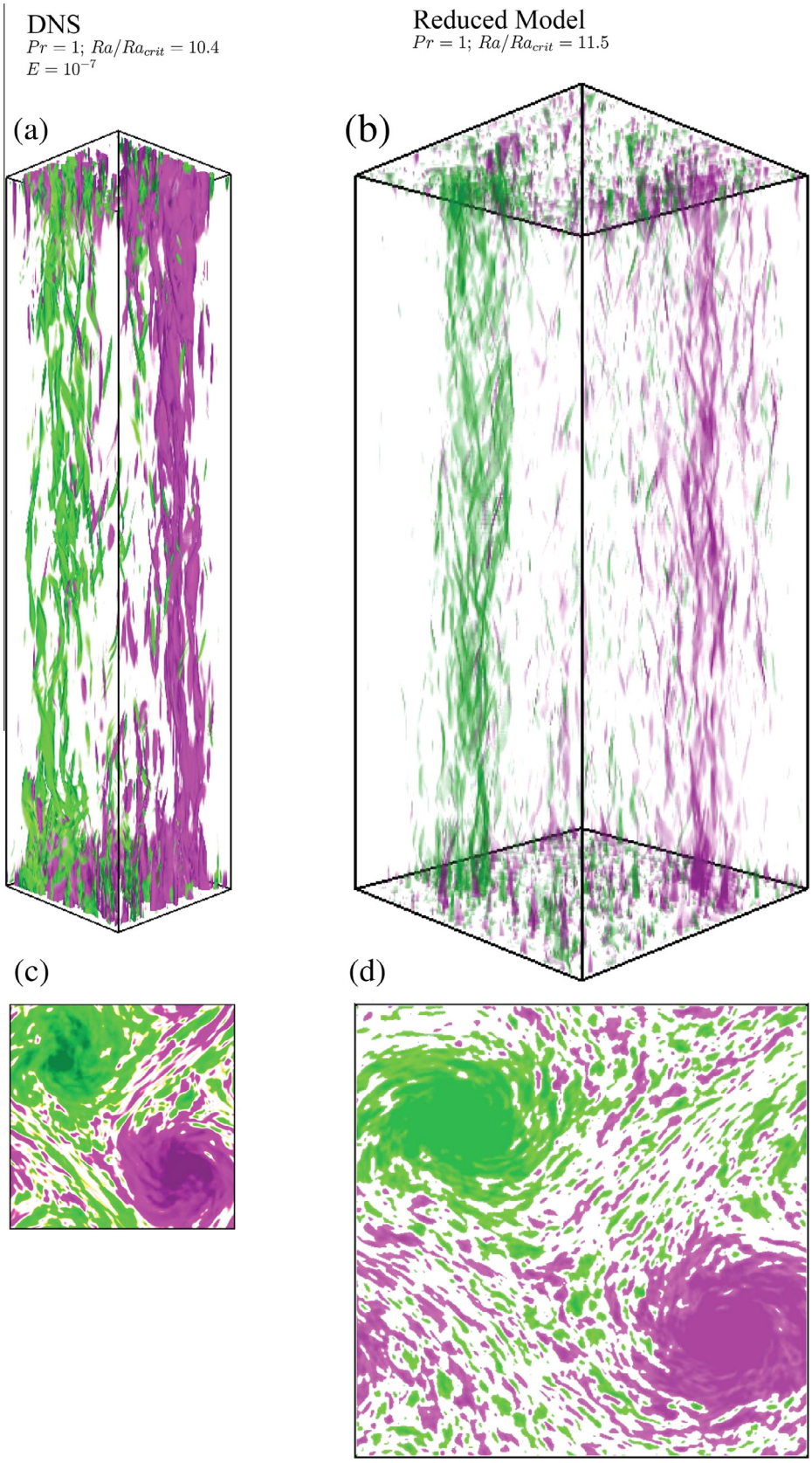


**Fig. 12.** Large-scale vortices (LSVs) in rotating, three-dimensional convection. (a) Rendering of axial vorticity field, $\zeta$, from free-slip DNS carried out at $E = 10^{-7}$, $Pr = 1$, $Ra/Ra_{crit} = 10.4$, and computational domain width $W \simeq 20\,\ell_{conv}$. Adapted from Stellmach et al. (2014). (b) Axial vorticity field from the reduced model carried out at $Pr = 1$, $Ra/Ra_{crit} = 11.5$, and $W \simeq 40\,\ell_{conv}$. Adapted from Rubio et al. (2014). (c and d) Axial integrations of $\zeta$ from panel a and b, respectively. The color scheme is the same as in Fig. 1c, but the scaling ranges all differ.

### 3.3. Large-scale coherent structures

Fig. 12 shows renderings of the axial vorticity fields, $\zeta$, from the free-slip DNS and reduced model carried out in the geostrophic turbulent regime, corresponding to the two rightmost cases displayed in Fig. 8. Figs. 12a and b show 3D renderings of the axial vorticity field. Two counter-rotating, large-scale vortices (LSVs) form in each computational domain; they extend axially across the entire domain, embedded within a sea of small-scale geostrophic turbulent structures. Figs. 12c and d show the $z$-integrated axial vorticity field, with both images dominated by the LSVs.

The widths, $W$, of the reduced computational domain is twice that of the DNS cases presented here. This difference allows us to test the effect of box size on the saturation scale of Cartesian LSVs. Comparing Figs. 12c and d shows that the LSVs grow until they roughly fill the entire computational domain (e.g., Julien et al., 2012b). Thus, the larger the domain, the larger the scale at which the LSVs saturate.

Given sufficiently turbulent, rapidly rotating convection, LSVs have been found to develop in an array of recent high resolution numerical models in stress-free, doubly-periodic domains (e.g., Käpylä et al., 2011; Chan and Mayr, 2013; Favier et al., 2014; Guervilly et al., 2014; Stellmach et al., 2014; Rubio et al., 2014) and triply-periodic domains (e.g., Mininni and Pouquet, 2010). (See also Sreenivasan and Jones (2006a) for magnetically-enhanced high latitude vortices in a planetary dynamo model.) In the survey by Favier et al. (2014), it was found that LSVs formed only in cases with $Re_\ell \gtrsim 20$ and $Ro_\ell \lesssim 1$. Thus, it was found that for overly small local Reynolds numbers, too few modes were available to take part in nonlinear energy exchanges; for overly large local Rossby numbers, the turbulence was effectively isotropic and had no preferred directionality.

It must be stressed that most of the energy in these flows is dissipated by viscosity on small scales (a standard, forward energy cascade), and that only a fraction is transferred non-locally to the large-scale, axial vorticity (an inverse energy cascade). LSVs, therefore, form *slowly* via the nearly inviscid pile-up of energy into large-scale, quasi-two-dimensional, axially-invariant modes. Thus, both low Ekman number values (such that $Ro = ReE \ll 1$) and long time scale experiments are required for significant energy to accumulate in LSV modes (e.g., Julien et al., 2012b). They will not be able to develop in experiments that are integrated on shorter time scales comprising a moderate number of advective turnover times. This behavior is similar to studies of QG zonal flows in spherical shells, in which sufficiently long integration times are necessary for the zonal velocity field to become fully developed (cf. Sun et al., 1993; Christensen, 2001).

The fact that LSVs form in Rubio et al. (2014)'s reduced models demonstrates that LSVs can be generated by rotating convective turbulence even in the theoretical limit of low Rossby number. In fact, this reduced modeling result then suggests that LSVs are capable of forming even at the very low Rossby number values that describe planetary core flows. Additionally, the essential agreement between $E = 10^{-7}$, $Pr = 1$ stress-free DNS and $Pr = 1$ reduced modeling results verifies that the reduced equations are predictive of strongly nonlinear, low $Ro$, high $Re$ solutions of the full Navier–Stokes equations.

The effects of LSVs on convective heat transfer are not well understood. In the moderate Rossby number simulations of Favier et al. (2014) and Guervilly et al. (2014), they find that the presence of LSVs weakly decreases the convective heat transfer efficiency across the fluid layer. In contrast, the reduced models of Rubio et al. (2014) find a slight increase in $Nu$ when LSVs are present. Thus, the generalized mechanism by which LSVs alter the convective heat transfer has yet to be clearly elucidated.

To date, convection-driven LSVs have not been found in laboratory experiments or in DNS with non-slip boundary conditions (Stellmach et al., 2014). However, inverse energy cascades have been detected in rapidly-rotating laboratory experiments with forced turbulence (e.g., Yarom et al., 2013), suggesting that convection-driven LSVs will be detected in laboratory experiments and in non-slip DNS that are carried out at sufficiently extreme conditions (e.g., $E \lesssim 10^{-7}$, $Pr \lesssim 1$).

## 4. Extrapolations and predictions

In the previous section, we presented the results of our state-of-the-science laboratory-numerical-theoretical models of high latitude planetary core-style hydrodynamic rotating convection, made in cylindrical tanks and doubly-periodic Cartesian domains. Our main findings are the following. (*i*) Convective heat transfer is efficient in high latitude geometries in which the gravity and rotation vectors are aligned, with especially efficient heat transfer occurring in the presence of non-slip horizontal boundaries. (*ii*) Columnar convection in $Pr \sim 1$ fluids tends to break down into anisotropic, 3D, geostrophic turbulent flow in the vicinity of $Ra/Ra_{crit} = O(10)$ for all three methods and irrespective of the mechanical boundary conditions. (*iii*) Cartesian, 3D geostrophic turbulence generates a weak flux of kinetic energy into system-scale, quasi-2D, columnar large-scale vortices (LSVs).

The theoretical investigations of Childress and Soward (1972); Soward (1974) and Calkins et al. (2015b) show that dynamo action can be driven by quasi-geostrophic convective flows. Bearing this in mind, in this section we extrapolate our rapidly-rotating, turbulent convection results to more extreme conditions in order to make predictions concerning the multi-scale nature of turbulence in planetary cores as well as in next-generation planetary dynamo models. In doing so, we will attempt to take into account what may be considered the leading order physics missing from our Cartesian models: the effects of spherical core geometry and magnetic field effects.

### 4.1. Geostrophic turbulent convection

We extrapolate our moderate Prandtl number heat transfer results to Earth's core conditions in Fig. 13. On the left hand side of the figure, the rotating convection data from Fig. 10a is plotted. On the right hand side, we plot the reduced modeling results for $E = 10^{-15}$, the typical $E$ estimate for Earth's outer core. In addition, the long dashed lines show extrapolations of both the steep $Pr \simeq 7$ non-slip heat transfer scaling law, $Nu \simeq (Ra/Ra_{crit})^{3.5}$, as well as the shallower reduced modeling trend, $Nu \simeq (Ra/Ra_{crit})^{3/2}$, both assuming $Ra_{crit}$ for $E = 10^{-15}$. Note that the $Pr = 1$ scaling in Stellmach et al. (2014) approximately bisects these two trends. In addition, we extrapolate the overarching $Nu \simeq Ra^{2/7}$ heat transfer branch to core conditions (e.g., Cheng et al., 2015).

Although rotating convective heat transfer is typically described in terms of $Nu$ and $Ra$, these quantities are difficult to constrain in deep planetary interiors since it is very difficult to estimate the superadiabatic temperature difference $\Delta\Theta$ across the core (e.g., Gubbins, 2001). Their product, though, which is called the flux Rayleigh number,

$$Ra_F = RaNu = \frac{\alpha g H^4 q_{sa}}{k\kappa\nu}, \tag{25}$$

does not depend on $\Delta\Theta$. This parameter can be estimated relatively accurately, for example, in Earth's core, because it depends only on the superadiabatic heat flux out from the core, $q_{sa}$, and the physical properties of the system. As explained in Cheng et al. (2015), conservative estimates of $Ra_F$ give its range in the core to be

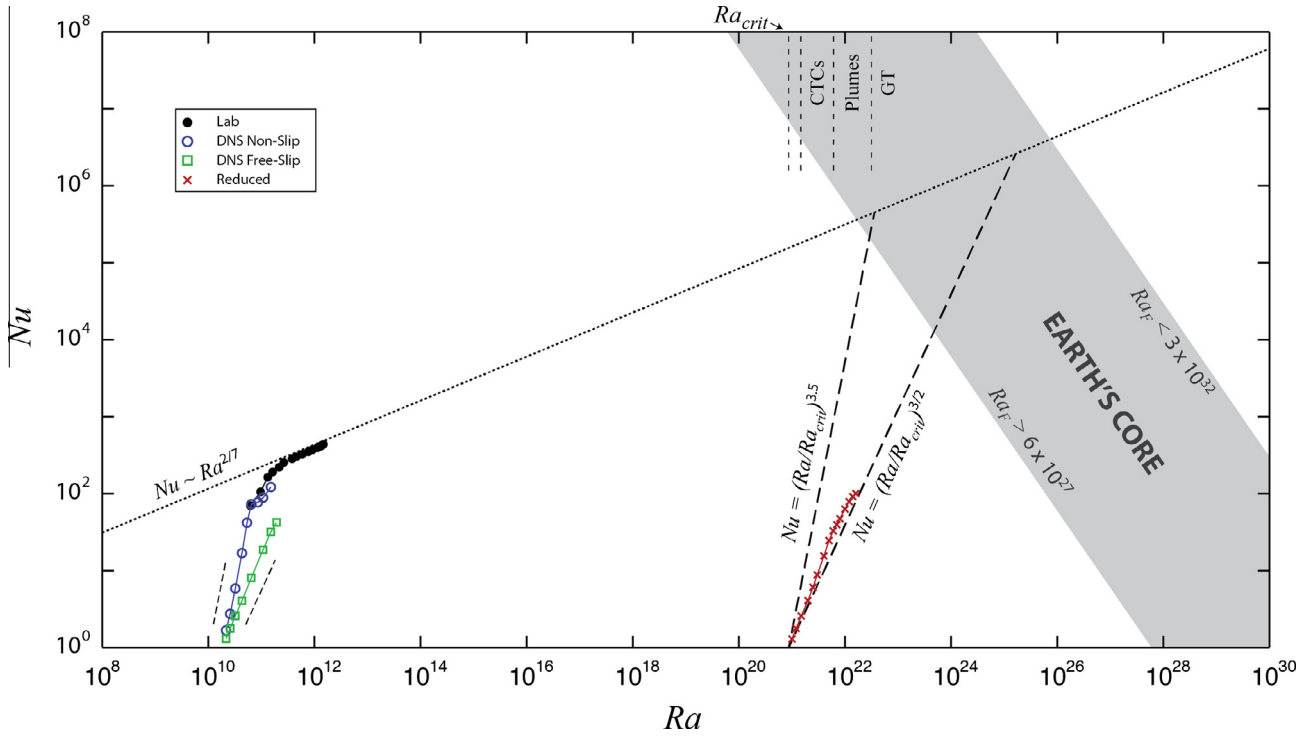


**Fig. 13.** Extrapolation of $Pr \simeq 7$, $Pm = 0$ laboratory/numerical/reduced heat transfer data in water to the estimated ranges of heat transfer parameters in Earth's liquid metal core where $Pr \simeq 10^{-1}$ to $10^{-2}$ and $Pm \simeq 10^{-6}$. On the left side of this figure, we plot laboratory and DNS *Nu*–*Ra* data. To the right, assuming $E = 10^{-15}$ as in Earth's core, we plot the two heat transfer scaling laws and the reduced modeling *Nu*–*Ra* data. The range of accessible *Nu*–*Ra* space for convection in Earth's core is denoted by the diagonal grey stripe on the figure's right side, corresponding to $6 \times 10^{27} \lesssim Ra_F \lesssim 6 \times 10^{32}$. Estimated flow regimes, defined in Sprague et al. (2006) and described in Fig. 9, are denoted cells (C), convective Taylor columns (CTCs), wavy plumes (P) and geostrophic turbulence (GT). Irrespective of the heat transfer scaling exponent, 3.5 or 1.5, the intersection with accessible $Ra_F$ values in Earth's core occurs in the geostrophic turbulence regime. Image adapted from Cheng et al. (2015).

$6 \times 10^{27} \lesssim Ra_F \lesssim 6 \times 10^{32}$. This $Ra_F$ range is shown as the diagonal grey stripe on the right side of Fig. 13.

Irrespective of the particular heat transfer scaling exponent, we find that our heat transfer extrapolations (the dashed lines) predominantly intersect the outer core $Ra_F$ estimates (the grey stripe) such that $Ra/Ra_{crit} \gtrsim 10$. Based on Fig. 9, this implies that (non-magnetic) rotating convective flows in Earth's core are not dominated by convective Taylor columns. Instead, this moderate *Pr* extrapolation suggests that convection exists in the geostrophic turbulence regime. Thus, our high latitude models of core convection suggest, in sharp contrast to the schematic views shown in Figs. 1d and 15a, that quasi-laminar columns are not prevalent under planetary core conditions.

At lower latitudes, situated well outside the tangent cylinder, we predict that low *E* convective flows will also occur in the form of 3D geostrophic turbulent motions. This argument stems from the asymptotically-reduced linear stability investigation of Calkins et al. (2013), in which it was found that many axially varying convection modes become accessible for $Ra < 10Ra_{crit}$ at moderate *Pr*.

Thus, based upon $Pr \simeq 7$ rotating convection results, we make the general prediction that convective flows in planetary cores, as well as in $E \lesssim 10^{-7}$ planetary dynamo models, will manifest predominantly in the form of 3D, geostrophic turbulence (cf. Nataf and Gagnière, 2008; Nataf and Schaeffer, 2015). This prediction can be tested using numerical model outputs: in the limit of strongly 3D geostrophic turbulence, the instantaneous axial coherence length-scale of the convection field will be far smaller than the system scale *H*. Instead, we hypothesize here that it will approach the scale of the thermal boundary layer thickness.

#### 4.1.1. Low Prandtl number considerations

The moderate *Pr* arguments above likely provide a conservative estimate for when convection columns become unstable to geostrophic turbulent motions. At lower *Pr* values, as describe core fluids, steady convective Taylor columns are never stable (Sprague et al., 2006). This trend is shown Fig. 9, in which the geostrophic turbulent regime is approaching the onset of convection as *Pr* is lowered. For example, Fig. 14 shows an oblique view of an

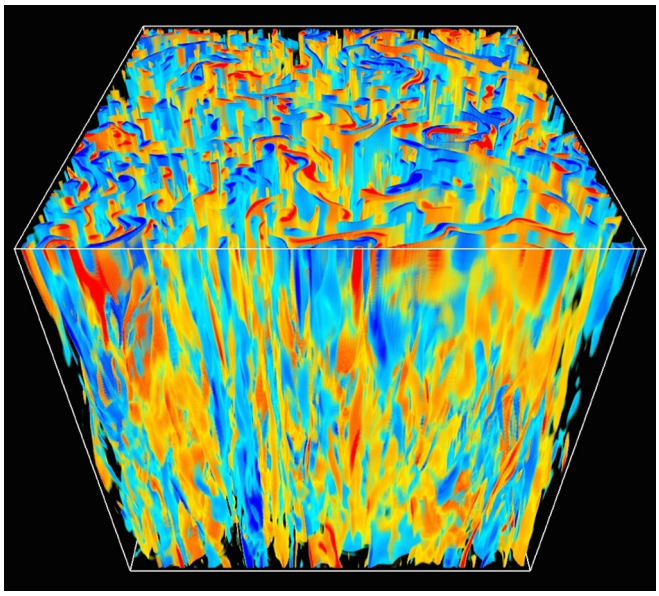

**Fig. 14.** Oblique view of the axial vorticity field in an asymptotically-reduced rotating convection model with $Pr = 0.0235$, a value comparable to that of many liquid metals. The flow is in the geostrophic turbulent regime, even though the $Ra = 1.0Ra_{crit}$ for steady cellular convection. Unlike previous reduced models, here we have set $\Gamma = 1$, in order to visually highlight axial variations in the vorticity field.

asymptotically-reduced model carried out at $Pr = 0.0235$, similar to that of liquid gallium and liquid mercury. The Rayleigh number in this case is set to the onset value for steady convection $Ra = Ra_{crit}$. This implies then that steady convective Taylor columns, which have a significant range of stability in moderate $Pr$ fluids, are not stable in low $Pr$ liquid metals.

Similarly, the laboratory-numerical simulations of rotating convection in liquid gallium made by Ribeiro et al. (2015) demonstrate that convection first onsets as *oscillatory* convection columns. These oscillatory columns become destabilized at $Ra \simeq 0.3 Ra_{crit}$ in cases with $E = 10^{-5}$ and $Pr \simeq 0.025$. Steady columnar convective motions, which are the dominant flow in most present-day dynamos, are not found. Thus, based upon low $Pr$ reduced models and Ribeiro et al. (2015)'s laboratory-numerical models, we predict that the regime of stable columns is far narrower in liquid metal convection than in the moderate $Pr$ simulations that have been the focus of this manuscript. In contrast to the extrapolation of our $Pr \simeq 7$ results in Fig. 13 to planetary core conditions, experiments in metals imply an even broader range of geostrophic turbulent convection in which columnar flows may never be stable.

### 4.2. Large-scale vortices

Space-filling axialized vortices develop in free-slip DNS and reduced modeling cases carried out in the geostrophic turbulent convection regime (Fig. 12). Based on our above arguments that geostrophic turbulent convection exists in Earth's core, we posit that LSVs can develop at high latitudes in Earth's core as well and may take part in the generation of high latitude geomagnetic flux patches.

In contrast, no high resolution studies have been carried out to date to investigate under what conditions LSVs can form at low latitudes where buoyancy forces predominantly act in the direction perpendicular to the rotation axis. In this "low latitude" configuration, convection often drives large-scale zonal jet flows (e.g., Christensen, 2001; Heimpel et al., 2005; Gillet et al., 2007). It is unclear whether LSVs in deep fluid layers can co-exist with zonal flows or whether they are subsumed by the zonal jet generation processes.

We will assume here that LSVs are able to form at all latitudes in planetary cores. However, unlike in Cartesian boxes where LSVs grow to the size of the computational domain, in planetary cores their growth should halt approximately at the Rhines scale, denoted as $\ell_{turb}$, where boundary curvature effects act to truncate the inverse energy cascade (e.g., Vasavada and Showman, 2005). Applying the spherical shell topographic Rhines scaling arguments of Heimpel and Aurnou (2007) yields

$$\ell_{turb} \simeq \pi r_c \left( Ro \left[ \frac{\chi^2 - \cos^2\beta}{\sin\beta \cos\beta} \right] \right)^{1/2} \quad \text{and} \quad \ell_{turb} \simeq \pi r_c (Ro/\cos\beta)^{1/2}, \tag{26}$$

where the left expression holds at high latitudes inside the tangent cylinder; the right expression holds at lower latitudes outside of the tangent cylinder; $r_c$ is the core radius; $\chi$ is the spherical shell radius ratio; and $\beta$ is the latitude angle in radians. In contrast to the laminar onset scale given by (9), the turbulent length-scales in (26) vary in proportion to the Rossby number; these turbulent scales are insensitive to the fluid viscosity. Thus, we predict that the small, convective length-scales in turbulent dynamo models will vary in proportion to the value of the Ekman number (e.g., the fluid viscosity), whereas the size of turbulent hydrodynamic structures will scale in proportion to the Rossby number (e.g., the fluid inertia).

Applying (26) to Earth's core and assuming an upper bounding estimate of $Ro \sim 10^{-5}$, we estimate that LSVs situated just outside the tangent cylinder at 69° latitude will halt their growth at a scale of roughly $\ell_{turb} \simeq 60$ km. This $\ell_{turb} \sim Ro^{1/2}$ turbulent length-scale exceeds the convective length scale $\ell_{conv} \sim E^{1/3}$ by a factor of approximately $10^3$, supporting our contention that a broad range of turbulent scales likely exist in planetary core flows. Hydrodynamic Rhines scales are still, however, far too small to provide a simple, direct explain for the 1000 km scale of the largest CMB geomagnetic flux patches.

### 4.3. Magnetohydrodynamic considerations

Extrapolating our hydrodynamic rotating convection results to planetary core settings has led us to argue that multi-scale processes arise, with 3D geostrophic turbulent at the convection scale and quasi-2D large-scale vortices on larger-scales. In Earth's core, upper bounding estimates for the local magnetic Reynolds number on the convection scale gives values that are less than unity:

$$Rm_{conv} \sim \frac{U \ell_{conv}}{\eta} = \frac{Ro\, Pm}{E^{2/3}} \sim \frac{10^{-5}\, 10^{-6}}{(10^{-15})^{2/3}} \sim 10^{-1}. \tag{27}$$

Using upper bounding values for the turbulent scale, $\ell_{turb} \sim \pi r_c Ro^{1/2}$ with $Ro \sim 10^{-5}$, leads to a magnetic Reynolds number that significantly exceeds unity:

$$Rm_{turb} \sim \frac{U \ell_{turb}}{\eta} \sim \frac{\pi Ro^{3/2}\, Pm}{E} \sim 10^2. \tag{28}$$

As stated before, the low value of $Rm_{conv}$ does not imply that dynamo generation processes cannot occur on the convection scale. As shown in a numerous theoretical investigations (e.g., Soward, 1974; Moffatt, 1978; Calkins et al., 2015b), in a multi-scale dynamo, small-scale motions act on the large-scale (locally-uniform) magnetic field to generate weak, small-scale emf's. The average of these weak, small-scale emf's creates, on the large-scale, a coherent current system that produces the large-scale magnetic field. Thus, the convection-scale magnetic field, although far weaker than the large-scale field, is a necessary component of the dynamo loop that connects the induction, and thereby the dynamics, of the small-scale convection with that of the large-scale magnetic field.

Guervilly et al. (2015) provide a recent example of dynamo generation driven by a turbulent rotating convective flow. Their numerical models solve Eqs. (1)–(3) in a Cartesian, doubly-periodic domain subject to stress-free, isothermal top and bottom boundary conditions. They argue that multi-scale turbulence develops in a $Pm = 0.2$ dynamo case. Further, they show that the dynamo threshold is lowered by the existence of an LSV that develops in this case. Guervilly et al. (2015)'s findings suggest then that $Pm$ must be lowered below unity in dynamo models in order for multi-scale turbulent processes to be able to develop. Thus, we hypothesize that multi-scale flows and multi-scale dynamo loops will emerge in next-generation, turbulent planetary dynamo models carried out at low $E$ and $Pm$.

## 5. Summary

We have presented the results of laboratory-numerical-theoretical models of rapidly rotating convection. These non-magnetic, Cartesian and cylindrical models provide novel predictions for the convective flows that will develop as global-scale models approach realistic planetary core conditions. Our results suggest that axially-coherent, helical, $\ell_{conv} \sim E^{1/3}$ convection columns break apart into three-dimensional geostrophic turbulence. Thus, we

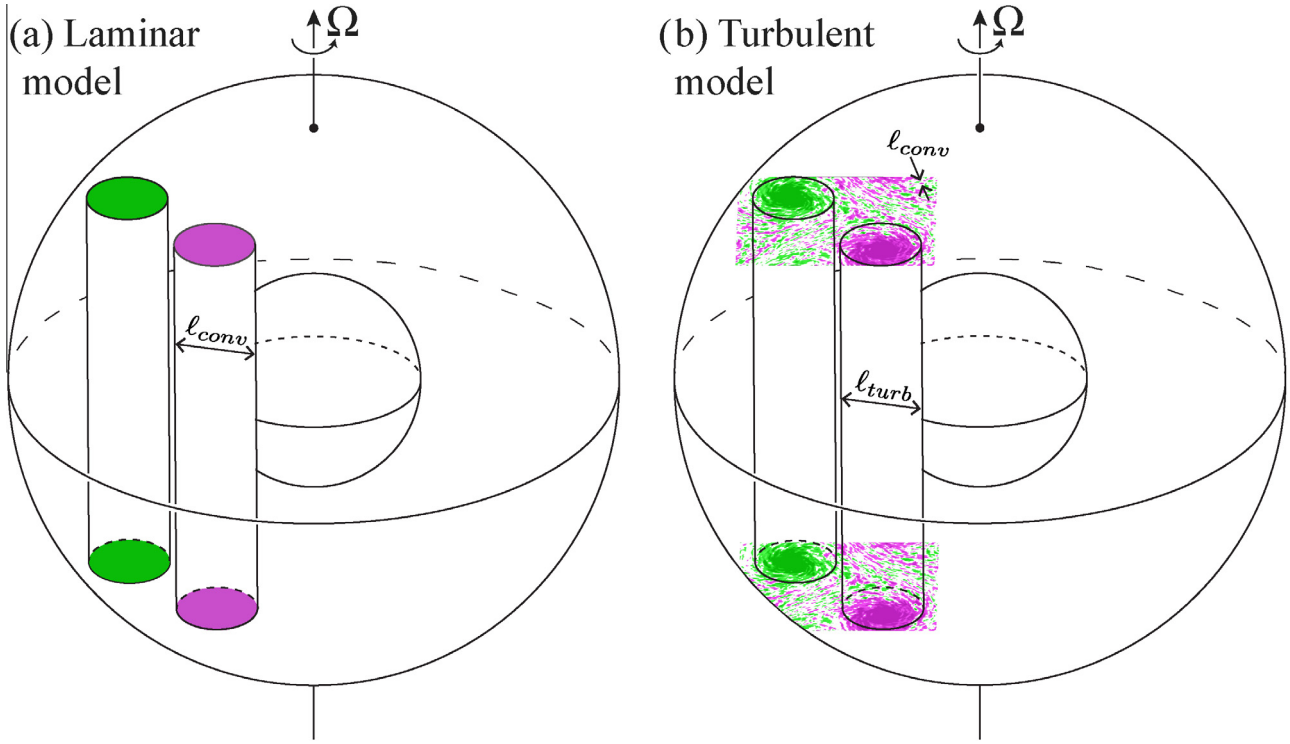


**Fig. 15.** (a) Schematic showing axial vorticity field in a present-day dynamo model containing laminar, axial convection columns. (b) Schematic showing *hypothetical* axial vorticity field in a multi-scale, rapidly-rotating turbulent planetary dynamo model. The convection scale $\ell_{conv}$ is far smaller than the system-scale in such models, and larger $\ell_{turb}$-scale structures form via turbulent processes. These large-scale structures can provide a novel way to generate system-scale crenelations in planetary magnetic fields and allow for different modes of dynamo action than are occurring in present-day quasi-laminar dynamo models.

argue that large-scale flows inferred to exist in planetary cores (e.g., Schaeffer and Pais, 2011) are not directly attributable to the columnar flows that develop near the onset of convection in present-day dynamo models (Fig. 15a). Furthermore, our results show that large-scale vortices (LSVs) develop on slow time scales in cases of geostrophic turbulent convective flow. These multiple scales of flows suggest that multi-scale dynamo processes can occur in planetary cores as well as in strongly turbulent, rapidly rotating dynamo models (Fig. 15b). Such multi-scale dynamo systems have long been proposed by theorists (e.g., Childress and Soward, 1972; Moffatt, 1978), but have yet to clearly emerge in global-scale planetary dynamo models.

Many open questions exist concerning the properties of LSVs in spherical geometries and in magnetohydrodynamic systems. For instance, it has yet to be shown that LSVs can form at low latitudes where significant horizontal (non-axial) buoyancy forces exist. To date, LSVs have been found to form in Cartesian, polar simulations subject to stress-free boundaries. These LSV flows are comprised of nearly perfectly horizontal motions with almost no helical component of flow. Even though these flows appear capable of generating substantial large-scale magnetic fields, it remains to be determined whether helical LSV flows develop in the presence of non-slip BCs or in fluid domains with boundary curvature.

To test the various mechanisms hypothesized for generating large-scale magnetic flux patches in Earth's core, we first need advanced models of the field itself (e.g., Lesur et al., 2008; Korte and Holme, 2010; Finlay et al., 2012). Given accurate field models, it is essential to generate advanced models of the essential turbulent processes and dynamo physics occurring in liquid metals. Efforts are being made in this direction via laboratory experiments (e.g., Cabanes et al., 2014; Zimmerman et al., 2014; Ribeiro et al., 2015). To computationally access turbulent liquid metal dynamo action, numerical models will need to be run on tens to hundreds of thousands of cores. Community dynamo codes will be capable of this in the next decade (http://geodynamics.org/). However, theoretical advances, such as the development of asymptotically reduced models of rotating convection and dynamo action in spherical shell geometries, may prove even more important for generating robust physical explanations of the turbulent dynamo action occurring in planetary cores.

## Acknowledgements

We gratefully acknowledge funding for this project from the US National Science Foundation (CSEDI award #1067944 and AST award #1067944) as well as the German Science Foundation (award #STE1976/1-2). Numerical simulations were carried out thanks to computing allocations from the John von Neuman Institute in Jülich and the NASA High-End Computing Program through the NASA Advanced Supercomputing Division at Ames Research Center. The reviews of three anonymous referees and discussions with Benjamin Favier greatly improved this manuscript. Finally, JMA thanks Judge Martin Herscovitz at the Van Nuys Courthouse West for providing the perfect venue for writing the first draft of this paper during jury service [not guilty].

## References

Anufriev, A.P., Jones, C.A., Soward, A.M., 2005. The Boussinesq and anelastic liquid approximations for convection in the Earths core. Phys. Earth Planet. Inter. 152, 163–190.
Aubert, J., Gillet, N., Cardin, P., 2003. Quasigeostrophic models of convection in rotating spherical shells. Geochem. Geophys. Geosys. 4, 1052.
Aubert, J., Aurnou, J.M., Wicht, J., 2008. The magnetic structure of convection-driven numerical dynamos. Geophys. J. Int. 172, 945–956.
Aubert, J., Finlay, C.C., Fournier, A., 2013. Bottom-up control of geomagnetic secular variation by the Earth's inner core. Nature 502, 219–223.

Aurnou, J.M., Andreadis, S., Zhu, L., Olson, P.L., 2003. Experiments on convection in Earth's core tangent cylinder. Earth Planet. Sci. Lett. 212, 119–134.

Bardóczi, L., Berta, M., Bencze, A., 2012. Inverse energy cascade and turbulent transport in a quasi-two-dimensional magnetized electrolyte system: An experimental study. Phys. Rev. E 85, 056315.

Barker, A., Dempsey, A.M., Lithwick, Y., 2014. Theory and simulations of rotation convection. Astrophys. J. 791, 13.

Bender, C.M., Orszag, S.A., 1999. Advanced Mathematical Methods for Scientists and Engineers I: Asymptotic Methods and Perturbation Theory. Springer-Verlag, Berlin.

Bloxham, J., 1986. The expulsion of magnetic flux from the Earth's core. Geophys. J.R. Astr. Soc. 87, 669–678.

Bloxham, J., Gubbins, D., 1987. Thermal core-mantle interactions. Nature 325, 511–513.

Buffett, B.A., 2014. Geomagnetic fluctuations reveal stable stratification at the top of the Earth's core. Nature 507, 484–487.

Busse, F.H., 1970. Thermal instabilities in rapidly rotating systems. J. Fluid Mech. 44, 441–460.

Cabanes, S., Schaeffer, N., Nataf, H.-C., 2014. Turbulence reduces magnetic diffusivity in a liquid sodium experiment. Phys. Rev. Lett. 113, 184501.

Calkins, M.A., Aurnou, J.M., Eldredge, J.D., Julien, K., 2012. The influence of fluid properties on the morphology of core turbulence and the geomagnetic field. Earth Planet. Sci. Lett. 359, 55–60.

Calkins, M.A., Noir, J., Eldredge, J.D., Aurnou, J.M., 2012. The effects of boundary topography on convection in Earth's core. Geophys. J. Int. 189, 789–814.

Calkins, M.A., Julien, K., Marti, P., 2013. Three-dimensional quasi-geostrophic convection in the rotating cylindrical annulus with steeply sloping endwalls. J. Fluid Mech. 732, 214–244.

Calkins, M.A., Julien, K., Marti, P., 2014. Onset of rotating and non-rotating convection in compressible and anelastic ideal gases. Geophys. Astrophys. Fluid Dyn.

Calkins, M.A., Marti, P., Julien, K., 2015a. The breakdown of the anelastic approximation in rotating compressible convection: Implications for astrophysical systems. Proc. Roy. Soc. Lond. A 471, 20140689.

Calkins, M.A., Julien, K., Tobias, S., Aurnou, J.M., 2015b. A multiscale dynamo model driven by quasi-geostrophic convection. J. Fluid Mech., in press.

Cao, H., Aurnou, J.M., Wicht, J., Dietrich, W., Soderlund, K.M., Russell, C.T., 2014. A dynamo explanation of Mercury's anomalous magnetic field. Geophys. Res. Lett. 41.

Chan, K.L., Mayr, H.G., 2013. Numerical simulation of convectively generated vortices: Application to the Jovian planets. Earth Planet. Sci. Lett. 371, 212–219.

Chandrasekhar, S., 1961. Hydrodynamic and Hydromagnetic Stability. Oxford University Press, Oxford.

Cheng, J.S., Stellmach, S., Ribeiro, A., Grannan, A., King, E.M., Aurnou, J.M., 2015. Laboratory-numerical models of small-scale flows in planetary cores. Geophys. J. Int. 201, 1–17.

Childress, S., Soward, A.M., 1972. Convection-driven hydromagnetic dynamo. Phys. Rev. Lett. 29, 837–839.

Christensen, U.R., 2001. Zonal flow driven by deep convection in the major planets. Geophys. Res. Lett. 28, 2553–2556.

Christensen, U.R., 2002. Zonal flow driven by strongly supercritical convection in rotating spherical shells. J. Fluid Mech. 470, 115–133.

Christensen, U.R., 2010. Dynamo scaling laws and applications to the planets. Space Sci. Rev. 152, 565–590.

Christensen, U.R., 2011. Geodynamo models: Tools for understanding properties of Earth's magnetic field. Phys. Earth Planet. Inter. 187, 157–169.

Christensen, U.R., Aubert, J., 2006. Scaling properties of convection-driven dynamos in rotating spherical shells and application to planetary magnetic fields. Geophys. J. Int. 166, 97–114.

Christensen, U.R., Aubert, J., Hulot, G., 2010. Conditions for Earth-like geodynamo models. Earth Planet. Sci. Lett. 296, 487–496.

Cioni, S., Chaumat, S., Sommeria, J., 2000. Effect of a vertical magnetic field on turbulent Rayleigh-Bénard convection. Phys. Rev. E 62, R4520–R4523.

Davidson, P.A., 2004. Turbulence: An introduction for Scientists and Engineers. Oxford University Press, Oxford.

Davidson, P.A., 2013. Turbulence in Rotating. Stratified and Electrically Conducting Fluids. Cambridge University Press, Cambridge.

Dormy, E., Soward, A.M., Jones, C.A., Jault, D., Cardin, P., 2004. The onset of thermal convection in rotating spherical shells. J. Fluid Mech. 501, 43–70.

Ecke, R., Niemela, J., 2014. Heat transport in the geostrophic regime of rotating Rayleigh-Bénard convection. Phys. Rev. Lett. 113, 114301.

Favier, B., Proctor, M.R.E., 2013. Kinematic dynamo action in square and hexagonal patterns. Phys. Rev. E 88, 053011.

Favier, B., Silvers, L.J., Proctor, M.R.E., 2014. Inverse cascade and symmetry breaking in rapidly rotating Boussinesq convection. Phys. Fluids 26, 096605.

Finlay, C.C., Amit, H., 2011. On flow magnitude and field-flow alignment at Earths core surface. Geophys. J. Int. 186, 175–192.

Finlay, C.C., Jackson, A., Gillet, N., Olsen, N., 2012. Core surface magnetic field evolution 2000–2010. Geophys. J. Int. 189, 761–781.

Frisch, U., 1995. Turbulence: The Legacy of A.N. Kolmogorov. Cambridge University Press, Cambridge.

Gent, P.R., McWilliams, J.C., 1983. Consistent balanced models in bounded and periodic domains. Dynam. Atmos. Ocean. 7, 67–93.

Gillet, N., Brito, D., Jault, D., Nataf, H.-C., 2007. Experimental and numerical studies of convection in a rapidly rotating spherical shell. J. Fluid Mech. 580, 83–121.

Gilman, P.A., 1977. Nonlinear dynamics of Boussinesq convection in a deep rotating spherical shell - I. Geophys. Astrophys. Fluid Dyn. 8 (1), 93–135.

Glatzmaier, G.A., 2013. Introduction to modeling convection in planets and stars: Magnetic field, density stratification, rotation. Princeton Ser. Astrophy.

Glatzmaier, G.A., Evonuk, M., Rogers, T., 2009. Differential rotation in giant planets maintained by density-stratified turbulent convection. Geophys. Astrophys. Fluid Dyn. 103 (1), 31–51.

Greenspan, H.P., 1968. The Theory of Rotating Fluids. Cambridge University Press, London.

Grooms, I., Julien, K., Weiss, J.B., Knobloch, E., 2010. Model of convective Taylor columns in rotating Rayleigh-Benard convection. Phys. Rev. Lett. 104, 224501.

Gubbins, D., 2001. The Rayleigh number for convection the Earth's core. Phys. Earth Planet. Inter. 128, 3–12.

Gubbins, D., Richards, M.A., 1986. Coupling of the core dynamo and mantle: Thermal or topographic? Geophys. Res. Lett. 13, 1521–1524.

Gubbins, D., Masters, G., Nimmo, F., 2008. A thermochemical boundary layer at the base of Earth's outer core and independent estimate of core heat flux. Geophys. J. Int. 174, 1007–1018.

Guervilly, C., Hughes, D.W., Jones, C.A., 2014. Large-scale vortices in rapidly rotating Rayleigh-Bénard convection. J. Fluid Mech. 758, 407–435.

Guervilly, C., Hughes, D.W., Jones, C.A., 2015. Generation of magnetic fields by large-scale vortices in rotating convection. Phys. Rev. E 91, 041001.

Heimpel, M.H., Aurnou, J.M., 2007. Turbulent convection in rapidly rotating spherical shells: A model for equatorial and high latitude jets on Jupiter and Saturn. Icarus 187, 540–555.

Heimpel, M., Aurnou, J., Wicht, J., 2005. Simulation of equatorial and high-latitude jets on Jupiter in a deep convection model. Nature 438, 193–196.

Hori, K., Wicht, J., Christensen, U.R., 2012. The influence of thermo-compositional boundary conditions on convection and dynamos in a rotating spherical shell. Phys. Earth Planet. Inter. 196–197, 32–48.

Ishihara, N., Kida, S., 2002. Dynamo mechanism in a rotating spherical shell: competition between magnetic field and convective vortices. J. Fluid Mech. 465, 1–32.

Jackson, A., 2003. Intense equatorial flux spots on the surface of the Earth's core. Nature 424, 760–763.

Johnson, C.L., Constable, C.G., 1998. Persistently anomalous Pacific geomagnetic fields. Geophys. Res. Lett. 25, 1011–1014.

Johnston, H., Doering, C.R., 2009. Comparison of turbulent thermal convection between conditions of constant temperature and constant flux. Phys. Rev. Lett. 102, 064501.

Jones, C.A., 2011. Planetary magnetic fields and fluid dynamos. Ann. Rev. Fluid Mech. 43, 583–614.

Jones, C.A., 2014. A dynamo model of Jupiters magnetic field. Icarus 241, 148–159.

Julien, K., Knobloch, E., 1998. Strongly nonlinear convection cells in a rapidly rotating fluid layer: the tilted f-plane. J. Fluid Mech. 360, 141–178.

Julien, K., Knobloch, E., 2007. Reduced models for fluid flows with strong constraints. J. Math. Phys. 48, 065405.

Julien, K., Legg, S., McWilliams, J., Werne, J., 1996. Rapidly rotating turbulent Rayleigh-Bénard convection. J. Fluid Mech. 322, 243–273.

Julien, K., Knobloch, E., Werne, J., 1998. A new class of equations for rotionally constrained flows. Theoret. Comput. Fluid Dynamics 11, 251–261.

Julien, K., Knobloch, E., Milliff, R., Werne, J., 2006. Generalized quasi-geostrophy for spatially anisotropic rotationally constrained flows. J. Fluid Mech. 555, 233–274.

Julien, K., Knobloch, E., Rubio, A.M., Vasil, G.M., 2012a. Heat transport in low Rossby number Rayleigh-Bénard convection. Phys. Rev. Lett. 109, 254503.

Julien, K., Rubio, A.M., Grooms, I., Knobloch, E., 2012b. Statistical and physical balances in low Rossby number Rayleigh-Bénard convection. Geophys. Astrophys. Fluid Dyn. 4–5, 392–428.

Julien, K., Aurnou, J.M., Calkins, M.A., Knobloch, E., Marti, P., Stellmach, S., Vasil, G.M., 2015. A nonlinear composite reduced model for rotationally constrained convection with Ekman pumping. J. Fluid Mech, submitted for publication.

Kageyama, A., Sato, T., 1997. Generation mechanism of a dipole field by a magnetohydrodynamic dynamo. Phys. Rev. E 55, 4617–4626.

Käpylä, P.J., Korpi, M.J., Hackman, T., 2011. Starspots due to large-scale vortices in rotating turbulent convection. Astrophys. J. 742, 34–41.

Kaspi, Y., Flierl, G.R., Showman, A.P., 2009. The deep wind structure of the giant planets: Results from an anelastic general circulation model. Icarus 202, 525–542.

King, E.M., Aurnou, J.M., 2012. Thermal evidence of Taylor columns in turbulent rotating Rayleigh-Bénard convection. Phys. Rev. E 85, 016313.

King, E.M., Aurnou, J.M., 2013. Turbulent convection in liquid metal with and without rotation. Proc. Natl. Acad. Sci. USA 110, 6688–6693.

King, E.M., Aurnou, J.M., 2015. Magnetostrophic balance as the optimal state for turbulent magnetoconvection. Proc. Natl. Acad. Sci. USA 112, 990–994.

King, E.M., Buffett, B.A., 2013. Flow speeds and length scales in geodynamo models: The role of viscosity. Earth Planet. Sci. Lett. 371–372, 156–162.

King, E.M., Stellmach, S., Noir, J., Hansen, U., Aurnou, J.M., 2009. Boundary layer control of rotating convection systems. Nature 457, 301–304.

King, E.M., Stellmach, S., Aurnou, J.M., 2012. Heat transfer by rapidly rotating Rayleigh-Bénard convection. J. Fluid Mech. 691, 568–582.

King, E.M., Stellmach, S., Buffett, B.A., 2013. Scaling behavior in Rayleigh-Bénard convection with and without rotation. J. Fluid Mech. 717, 449–471.

Korte, M., Holme, R., 2010. On the persistence of geomagnetic flux lobes in global Holocene field models. Phys. Earth Planet. Inter. 182, 179–186.

Kunnen, R.P.J., Clercx, H.J.H., Geurts, B.J., 2006. Heat flux intensification by vortical flow localization in rotating convection. Phys. Rev. E 74, 056306.

Lesur, V., Wardinski, I., Rother, M., Mandea, M., 2008. GRIMM: the GFZ Reference Internal Magnetic Model based on vector satellite and observatory data. Geophys. J. Int. 173, 382–394.

Livermore, P.W., Hollerbach, R., Jackson, A., 2013. Electromagnetically driven westward drift and inner-core superrotation in Earth's core. Proc. Natl. Acad. Sci. USA 110, 15914–15918.
Matsui, H., King, E.M., Buffett, B.A., 2014. Multiscale convection in a geodynamo simulation with uniform heat flux along the outer boundary. Geochem. Geophys. Geosys. 15, 3212–3225.
McWilliams, J.C., 1984. The emergence of isolated coherent vortices in turbulent flow. J. Fluid Mech. 146, 21–43.
McWilliams, J.C., 2012. The elemental shear dynamo. J. Fluid Mech. 699, 414–452.
Mininni, P.D., Pouquet, A., 2010. Rotating helical turbulence. II. Intermittency, scale invariance, and structures. Phys. Fluids 22, 025104.
Moffatt, H.K., 1978. Magnetic Field Generation in Electrically Conducting Fluids. Cambridge University Press, Cambridge.
Nataf, H.-C., Gagnière, N., 2008. On the peculiar nature of turbulence in planetary dynamos. C.R. Physique 9, 702–710.
Nataf, H.-C., Schaeffer, N., 2015. Turbulence in the Core, vol. 8. Elsevier, NY, second ed., pp. 161–181.
Nayfeh, A.H., 1973. Perturbation Methods. John Wiley & Sons, New York.
Nieves, D., Rubio, A.M., Julien, K., 2014. Statistical classification of flow morphology in rapidly rotating Rayleigh-Bénard convection. Phys. Fluids 26, 086602.
Niiler, P.P., Bisshopp, F.E., 1965. On the influence of Corioles force on onset of thermal convection. J. Fluid Mech. 22, 753–761.
Olson, P.L., Amit, H., 2006. Changes in Earth's dipole. Naturwissenschaften 93, 519–542.
Olson, P.L., Christensen, U.R., Glatzmaier, G.A., 1999. Numerical modeling of the geodynamo: Mechanisms of field generation and equilibration. J. Geophys. Res. 104, 10383–10404.
Ouellette, N.T., 2012. Turbulence in two dimensions. Phys. Today 65 (5), 68–69.
Pais, A., Jault, D., 2008. Quasi-geostrophic flows responsible for the secular variation of the Earth's magnetic field. Geophys. J. Int. 173.
Pozzo, M., Davies, C., Gubbins, D., Alfe, D., 2012. Thermal and electrical conductivity of iron at Earth's core conditions. Nature 485. http://dx.doi.org/10.1038/nature11031.
Ribeiro, A., Guermond, J.-L., Fabre, G., Aurnou, J.M., 2015. Canonical models of geophysical and astrophysical flows: Turbulent convection experiments in liquid metals. Metals 5, 289–335.
Roberts, P.H., King, E.M., 2013. On the genesis of the Earth's magnetism. Rev. Prog. Phys. 76, 096801.
Rubio, A.M., Julien, K., Knobloch, E., Weiss, J.B., 2014. Upscale energy transfer in three-dimensional rapidly rotating turbulent convection. Phys. Rev. Lett. 112, 144501.
Sakuraba, A., Roberts, P.H., 2009. Generation of a strong magnetic field using uniform heat flux at the surface of the core. Nature Geosci. 2, 802–805.
Schaeffer, N., Cardin, P., 2006. Quasi-geostrophic kinematic dynamos at low magnetic Prandtl number. Earth Planet. Sci. Lett. 245, 595–604.
Schaeffer, N., Pais, M.A., 2011. On symmetry and anisotropy of Earth-core flows. Geophys. Res. Lett. 38, L10309.
Schubert, G., Soderlund, K.M., 2011. Planetary magnetic fields: observations and models. Phys. Earth Planet. Inter. 187, 92–108.
Sheyko, A.A., 2014. Numerical Investigations of Rotating MHD in a Spherical Shell (Ph.D. thesis). ETH Zurich.
Soderlund, K.M., King, E.M., Aurnou, J.M., 2012. The influence of magnetic fields in planetary dynamo models. Earth Planet. Sci. Lett. 333–334, 9–20.
Soward, A.M., 1974. A convection-driven dynamo: I. The weak field case. Phil. Trans. Roy. Soc. Lond. A 275, 611–646.
Sprague, M., Julien, K., Knobloch, E., Werne, J., 2006. Numerical simulation of an asymptotically reduced system for rotationally constrained convection. J. Fluid Mech. 551, 141–174.
Sreenivasan, B., 2010. Modelling the geodynamo: progress and challenges. Curr. Sci. 99, 1739–1750.
Sreenivasan, B., Jones, C.A., 2006a. Azimuthal winds, convection and dynamo action in the polar regions of planetary cores. Geophys. Astrophys. Fluid Dyn. 100, 319–339.
Sreenivasan, B., Jones, C.A., 2006b. The role of inertia in the evolution of spherical dynamos. Geophys. J. Int. 164, 467–476.
Sreenivasan, B., Sahoo, S., Dhama, G., 2014. The role of buoyancy in polarity reversals of the geodynamo. Geophys. J. Int. 199, 1698–1708.
Stanley, S., Glatzmaier, G.A., 2010. Dynamo models for planets other than Earth. Space Sci. Rev. 152, 617–649.
Stellmach, S., Hansen, U., 2004. Cartesian convection driven dynamos at low Ekman number. Phys. Rev. E 70, 056312.
Stellmach, S., Hansen, U., 2008. An efficient spectral method for the simulation of dynamos in Cartesian geometry and its implementation on massively parallel computers. Geochem. Geophys. Geosys. 9. http://dx.doi.org/10.1029/2007GC001778.
Stellmach, S., Lischper, M., Julien, K., Vasil, G., Cheng, J.S., Ribeiro, A., King, E.M., Aurnou, J.M., 2014. Approaching the asymptotic regime of rapidly rotating convection: Boundary layers vs. interior dynamics. Phys. Rev. Lett. 113, 254501.
Stewartson, K., Cheng, H.K., 1979. On the structure of inertial waves produced by an obstacle in a deep, rotating container. J. Fluid Mech. 91, 415–432.
Sun, Z.-P., Schubert, G., Glatzmaier, G.A., 1993. Banded surface flow maintained by convection in a model of the rapidly rotating giant planets. Science 260, 661–664.
Takahashi, F., Shimizu, H., 2012. A detailed analysis of a dynamo mechanism in a rapidly rotating spherical shell. J. Fluid Mech. 701, 228–250.
Tritton, D.J., 1988. Physical Fluid Dynamics. Oxford University Press, Oxford.
Vallis, G.K., 2006. Atmospheric and Oceanic Fluid Dynamics. Cambridge University Press, Cambridge.
Vasavada, A.R., Showman, A.P., 2005. Jovian atmospheric dynamics: an update after Galileo and Cassini. Rev. Prog. Phys. 68, 1935–1996.
Verhoeven, J., Stellmach, S., 2014. The compressional beta effect: A source of zonal winds in planets? Icarus 237, 143–158.
Veronis, G., 1959. Cellular convection with finite amplitude in a rotating fluid. J. Fluid Mech. 5, 401–435.
Yarom, E., Vardi, Y., Sharon, E., 2013. Experimental quantification of inverse energy cascade in deep rotating turbulence. Phys. Fluids 25, 085105.
Zhang, K., Schubert, G., 2000. Magnetohydrodynamics in rapidly rotating spherical systems. Ann. Rev. Fluid Mech. 32, 409–443.
Zhong, J.-Q., Stevens, R.J.A.M., Clercx, H.J.H., Verzicco, R., Lohse, D., Ahlers, G., 2009. Prandtl-, Rayleigh-, and Rossby-number dependence of heat transport in turbulent rotating Rayleigh-Bénard convection. Phys. Rev. Lett. 102, 044502.
Zimmerman, D.S., Triana, S.A., Lathrop, D.P., 2011. Bi-stability in turbulent, rotating spherical Couette flow. Phys. Fluids 23, 065104.
Zimmerman, D.S., Triana, S.A., Nataf, H.-C., Lathrop, D.P., 2014. A turbulent, high magnetic Reynolds number experimental model of Earth's core. J. Geophys. Res. 119, 4538–4557.